Received: 16 August 2021 | Revised: 14 October 2021 | Accepted: 24 October 2021

DOI: 10.1002/inf2.12290

REVIEW ARTICLE

WILEY

Interfacial charge and energy transfer in van der Waals heterojunctions

Zehua Hu[1] | Xue Liu[2] | Pedro Ludwig Hernández-Martínez[3] | Shishu Zhang[4] | Peng Gu[5] | Wei Du[6] | Weigao Xu[7] | Hilmi Volkan Demir[3,8] | Haiyun Liu[5] | Qihua Xiong[4,5,9]

[1]Division of Physics and Applied Physics, School of Physical and Mathematical Sciences, Nanyang Technological University, Singapore, Singapore

[2]Institutes of Physical Science and Information Technology, Anhui University, Hefei, P.R. China

[3]LUMINOUS! Center of Excellence for Semiconductor Lighting and Display, School of Electrical and Electronics Engineering, Nanyang Technological University, Singapore, Singapore

[4]State Key Laboratory of Low-Dimensional Quantum Physics, Department of Physics, Tsinghua University, Beijing, P.R. China

[5]Beijing Academy of Quantum Information Sciences, Beijing, P.R. China

[6]Institute of Functional Nano and Soft Materials (FUNSOM), Soochow University, Suzhou, P.R. China

[7]Key Laboratory of Mesoscopic Chemistry of MOE, School of Chemistry and Chemical Engineering, Nanjing University, Nanjing, P.R. China

[8]Department of Physics, Department of Electrical and Electronics Engineering, UNAM-National Nanotechnology Research Center and Institute of Materials Science and Nanotechnology, Bilkent University, Ankara, Turkey

[9]Beijing Innovation Center for Future Chips, Tsinghua University, Beijing, P.R. China

Correspondence
Qihua Xiong, State Key Laboratory of Low-Dimensional Quantum Physics, Department of Physics, Tsinghua University, Beijing 100084, P.R. China.
Email: qihua_xiong@tsinghua.edu.cn

Zehua Hu, Division of Physics and Applied Physics, School of Physical and Mathematical Sciences, Nanyang Technological University, Singapore 637371, Singapore.
Email: zehua.hu@ntu.edu.sg

Haiyun Liu, Beijing Academy of Quantum Information Sciences, Beijing 100193, P.R. China.
Email: liuhy@baqis.ac.cn

Funding information
Agency for Science, Technology and Research, Grant/Award Number: 152 73 00025; Central University Basic Research Fund of China, Grant/Award Numbers: 020514380231, 021014380177;

Abstract

Van der Waals heterojunctions are fast-emerging quantum structures fabricated by the controlled stacking of two-dimensional (2D) materials. Owing to the atomically thin thickness, their carrier properties are not only determined by the host material itself, but also defined by the interlayer interactions, including dielectric environment, charge trapping centers, and stacking angles. The abundant constituents without the limitation of lattice constant matching enable fascinating electrical, optical, and magnetic properties in van der Waals heterojunctions toward next-generation devices in photonics, optoelectronics, and information sciences. This review focuses on the charge and energy transfer processes and their dynamics in transition metal dichalcogenides (TMDCs), a family of quantum materials with strong excitonic effects and unique valley properties, and other related 2D materials such as graphene and hexagonal-boron nitride. In the first part, we summarize the ultrafast charge transfer processes in van der Waals heterojunctions, including its experimental evidence and theoretical understanding, the interlayer excitons at the TMDC interfaces, and the hot carrier injection at the graphene/TMDCs interface. In the second

Zehua Hu, Xue Liu, and Pedro Ludwig Hernández-Martínez contributed equally to this work.

National Natural Science Foundation of China, Grant/Award Numbers: 12104006, 21873048, 92056204; National Research Foundation, Grant/Award Number: NRF-NRFI2016-08; Natural Science Foundation of Jiangsu Province, Grant/Award Number: BK20180319; Start up fundations from Anhui University; Tsinghua University; State Key Laboratory of Low-Dimensional Quantum Physics

part, the energy transfer, including both Förster and Dexter types, are reviewed from both experimental and theoretical perspectives. Finally, we highlight the typical charge and energy transfer applications in photodetectors and summarize the challenges and opportunities for future development in this field.

KEYWORDS

2-dimensional semiconductors, carrier dynamics, charge and energy transfer, optical spectroscopy, optoelectronics

1 | INTRODUCTION

Traditional bulk semiconducting heterojunctions such as those containing gallium arsenide (GaAs) quantum wells (QWs) are mainly prepared by molecular beam epitaxy, which is expensive and requires lattice-constant matching at the interface. In recent years, two-dimensional (2D) material has been discovered to possess weak van der Waals (vdWs) interlayer interaction, thereby readily scales down to a few-layer or even monolayer limit.[1] Today, tremendous 2D materials have been extensively studied, with various physical properties including metallic, semiconducting, and insulating aspects.[2] More interestingly, owing to their dangling-bond-free surfaces, they can be stacked together to form vdWs heterojunctions (Figure 1A), therefore having richer and much more tunable material properties.[4–6] Since the carrier wavefunction is delocalized and penetrates into adjacent layers, the carriers in the different layers could interact with each other, creating fascinating physical properties such as largely enhanced proximity effect and valley-polarized interlayer exciton. Moreover, the physical properties of the vdWs heterojunctions are tunable due to the susceptibility to the stacking order, crystal orientation alignments, electric/magnetic/optical field, strain, and temperature.[7–11]

The rise of vdWs heterojunction has ignited broad research interests into interfacial carrier dynamics as they are the bedrock of fundamental physics and optoelectronic applications. Interfacial carrier dynamics, including charge transfer (CT) and energy transfer (ET), are ubiquitous phenomena and essential processes that govern the interfacial properties of the vdWs heterojunctions. Although the interfacial carrier dynamics have been widely explored for several decades in various donor-acceptor systems such as organic semiconductor interface and biological molecules,[12,13] vdWs heterojunction is a brand new platform in the quantum limit with strong quantum confinement and coherence effect.

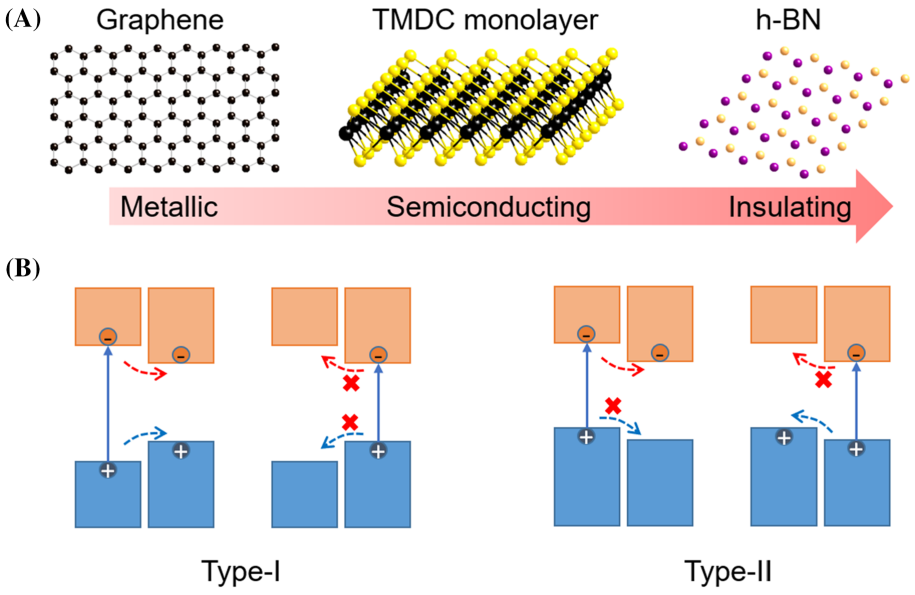

FIGURE 1 Typical 2D materials and the band alignment. (A) Typical 2D materials used for the building blocks of van der Waals heterojunctions. (B) Schematic of type-I and type-II band alignments and the allowed charge transfer (CT) directions, respectively. (B) Reproduced with permission from Reference 3. Copyright 2017, Royal Society of Chemistry

The carriers also feature the valley degree of freedom due to the spin-valley locking effect in transition metal dichalcogenides (TMDC) systems, thus expanding the carrier dynamics of electrons/holes into valley-dependent and setting the foundation for valleytronics.[14]

This review mainly discusses the carrier dynamics in TMDC vdWs heterojunctions as they are semiconductors with a sizable bandgap and strong excitonic effect.[15,16] Their individual physical properties have been extensively investigated theoretically and experimentally, which sets the foundation for heterojunction investigation. In the first part, we start by discussing the experimental evidence of ultrafast interfacial CT and the related theoretical understanding. Subsequently, the interlayer exciton that forms as a direct consequence of CT is summarized. The interlayer exciton attracts broad interest because it inherits the spin-valley locking effect from monolayer TMDC and has a much longer lifetime than intralayer exciton, showing great potential in valleytronics and exciton transistors. This part ends with a summary on CT at the graphene/TMDC interface, which exhibits rich physics because the hot carriers and plasmons in graphene are susceptible to the pump wavelength. In the second part on ET, both Förster and Dexter types are discussed. We first provide a comprehensive theoretical understanding of Förster resonance energy transfer (FRET) in vdWs heterojunctions and then focus on experimental progress. Notably, the spin-orbit-coupling-induced valence band splitting and high intrinsic doping make the individual exciton state quite complicated (such as B and C exciton, trion, and biexciton), so as the FRET dynamics. For Dexter-type energy transfer (DET), we emphasize the modulation of band alignment and the DET dynamics via an external electric field. In the subsequent part, we introduce a typical device application, that is, interlayer CT and ET enhanced photodetector. Finally, a summary and outlook are given toward the future development of CT and ET in vdWs heterojunctions.

2 | CT IN 2D MATERIAL HETEROJUNCTIONS

Thanks to the weak interlayer coupling between the interfaces, researchers usually consider the electronic states of 2D materials to approximately localize within individual layers, which is a similar treatment for interfaces between bulk materials and quantum wells.[17] In this case, one can effectively evaluate the band alignment according to the band edge energy of different layers.[18–20] As shown in Figure 1B, when the lowest occupied energy levels of electrons and holes reside in the same layer, a type-I band alignment is formed,[3] while they are separated in different layers for a type-II band alignment.[21] A type-III band alignment requires a much larger energy offset, that is, the conduction band minimum (CBM) in one layer is below the valence band maximum (VBM),[22] which is also possible in the 2D semiconductor family but is not the focus in this review. In the following, we describe experimental findings regarding the CT processes in 2D heterojunctions, including demonstrations, characterizations, and manipulations. Also, we briefly survey recent theoretical efforts on understanding the physical mechanisms of the ultrafast dynamics. Then, we highlight the exotic properties in TMDC/TMDC and TMDC/graphene heterojunctions due to the interlayer CT.

2.1 | Quantum coherence induced ultrafast CT

The energy offset between CBM or VBM provides the driving force to enable CT at 2D heterogeneous interfaces. Followed by this prerequisite, several experimental studies explored the CT processes in vertically stacked heterostructures, as shown in Figure 2A,B. Since the CT offers an additional relaxation channel between individual layers, the steady-state photoluminescence (PL) quenching of the constituent monolayers is typical.[23,27] Besides, the Raman scattering of graphene and TMDC monolayers exhibit specific dependence on their charge carrier density via electron–phonon coupling, that is, the G-mode of graphene upshifts or downshifts under the electron or hole doping, respectively[28–30]; the A_{1g} mode of TMDC monolayer is more sensitive to its doping level than other extrinsic factors such as strain, stress, and temperature.[31–35] Thus, a combination of PL and Raman scattering spectroscopies and their corresponding 2D spatial mappings are useful tools to systematically study the interlayer CT between graphene, hexagonal-boron nitride (h-BN), and TMDC monolayers.

For example, Guillaume et al. reported a photoinduced electron transfer from $MoSe_2$ to graphene and a hole accumulation in $MoSe_2$.[24] Their comprehensive analysis of the graphene and $MoSe_2$ Raman modes revealed that the graphene gets continually *n*-doped under the increasing incident photon flux and the Fermi energy of the graphene is saturated at ~290 meV above the Dirac point (Figure 2E–H). A detailed summary of the ultrafast carrier dynamics between graphene and TMDC will be given in Section 2.3. In addition, the transport properties of graphene, that is, the charge-neutral point determined by the resistance gate dependence, were used as a probe of the photoinduced CT between graphene and h-BN defect states due to its high sensivity to the doping

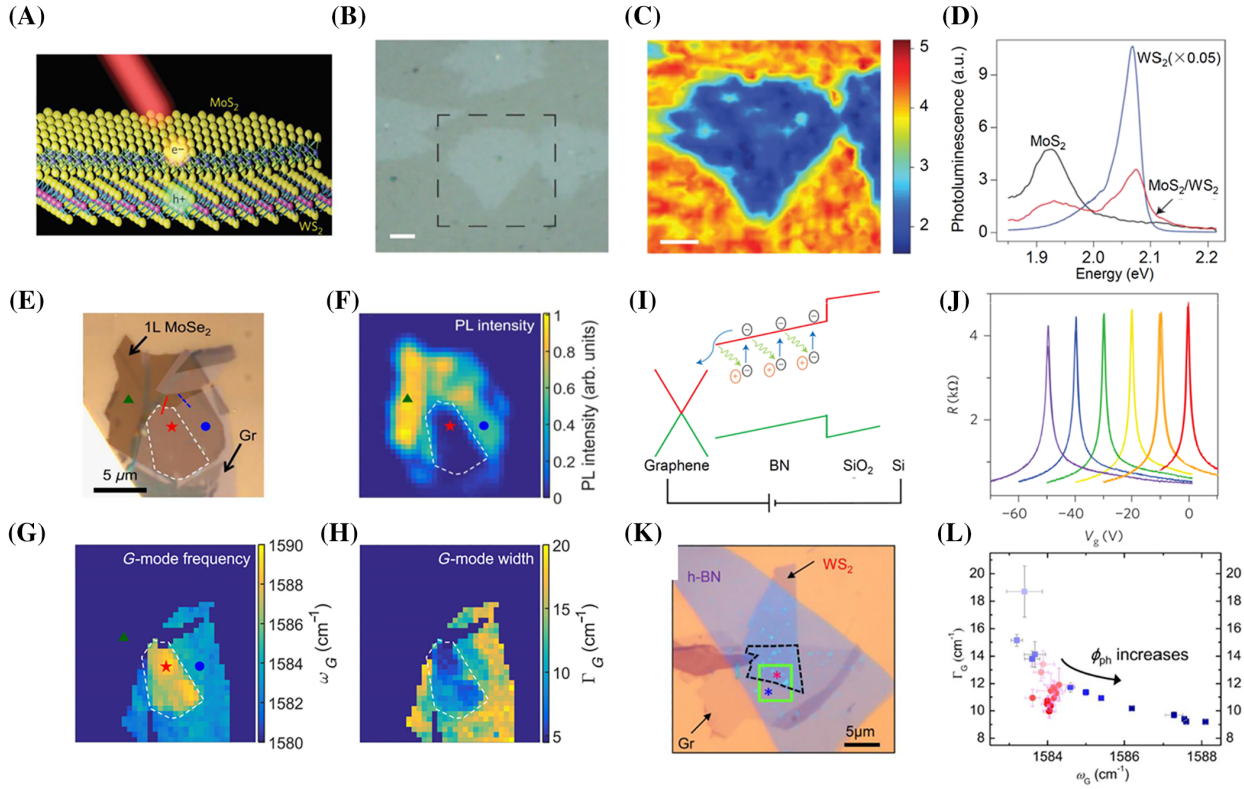

FIGURE 2 Interlayer charge transfer (CT) probed by static optical spectroscopies. (A–D) The schematic (A), optical image (B), PL mapping (C), and PL spectrum of a MoS_2/WS_2 heterostructure (D). (E–H) The optical image (E), PL mapping (F), graphene Raman G-mode frequency mapping (G), and G-mode width mapping (H) in a $MoSe_2$/graphene heterostructure. (I,J) Photoinduced doping effect in graphene/h-BN heterojunction in the schematic diagram (I), and demonstrated by the charge neutrality point shifting (J). The red trace is from the pristine sample, while the other traces are obtained after photodoping. (K,L) Manipulation of the CT between h-BN defect levels and graphene. (K) The optical image of the heterostructure containing WS_2/hBN/graphene and hBN/graphene regions. (L) Evolution of the Raman G-mode upon increasing photon flux in different regions. (A–D) Reproduced with permission from Reference 23. Copyright 2014, Nature Publishing group. (E–H) Reproduced with permission from Reference 24. Copyright 2018, American Physical Society. (I,J) Reproduced with permission from Reference 25. Copyright 2014, Nature Publishing group. (K,L) Reproduced with permission from Reference 26. Copyright 2020, American Physical Society

level.[25,36] From their observations, the donor-like defects in h-BN provide excited electrons in CB under optical excitation. These mobile electrons continuously transfer into the graphene with positively charged localized defects left in h-BN, introducing a screening effect to the back gate until graphene becomes charge-neutral (Figure 2I,J).[25] Moreover, in a sandwiched heterostructure, the manipulation of the CT between graphene and adjacent h-BN defect levels by adding or removing a top WS_2 layer was demonstrated (Figure 2K,L).[26] The donor-like defects in h-BN are utilized to provide defect excited states and ground states under optical excitation. Without a top WS_2 layer, the graphene was gradually n-doped until reaching a saturation Fermi energy of ~220 meV. However, by adding a top WS_2 layer, the doping level of graphene is no longer changed since a hole transfer from WS_2 to graphene also happens by the assistance of defect ground states in h-BN, which compensates the electron transfer and keeps graphene charge-neutral.[26] In contrast, on a weakly coupled WS_2/$MoSe_2$ heterojunction, the limited overlap of electronic wavefunctions across the heterojunctions (and the lack of interlayer phonon vibrations) promotes the interfacial quantum fluctuations, resulting in an exciting PL blinking phenomenon.[37] The PL intensities (and decay dynamics) of the two adjacent layers are always inversely correlated, that is, as one falls, another rises. These studies provide a comprehensive demonstration, understanding, and manipulation of CT between 2D systems.

Time-resolved pump-probe measurement is a powerful technique to elucidate the CT dynamics with femtosecond timescale resolution. Hong et al. first demonstrated a hole transfer from photoexcited 1L-MoS_2 to 1L-WS_2 using a combined PL mapping and ultrafast pump-probe spectroscopy method.[23] At the MoS_2/WS_2 overlapping region, the

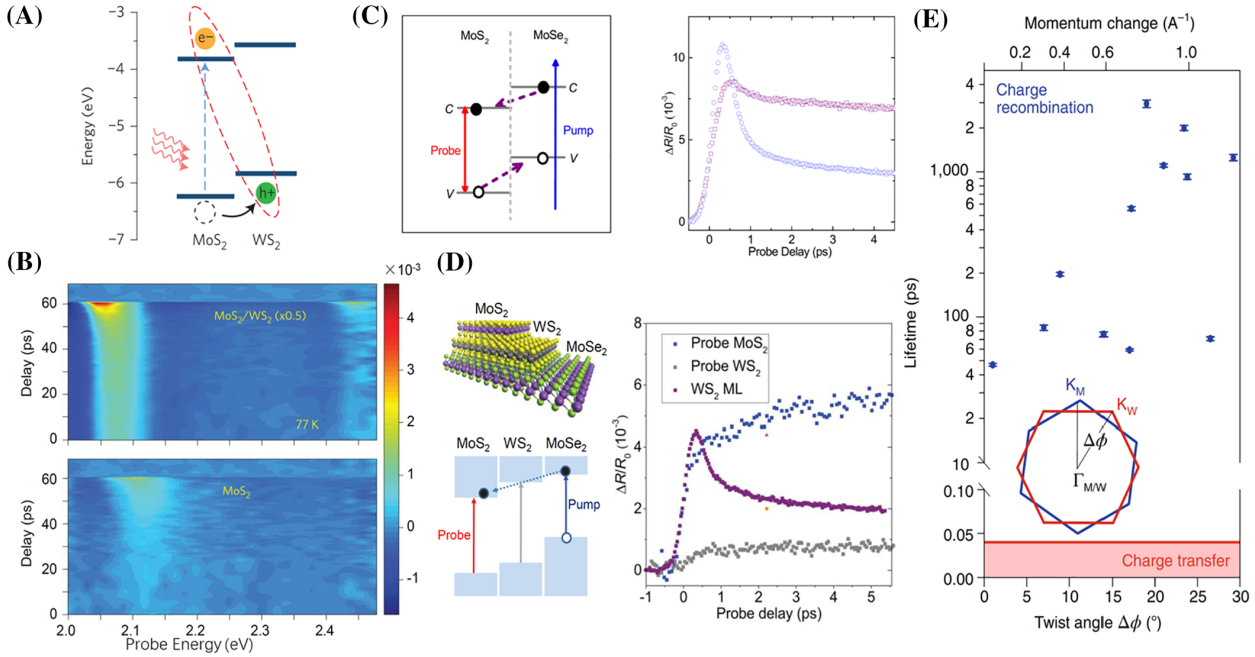

FIGURE 3 Interlayer charge transfer (CT) probed by pump-probe spectroscopies. (A) Schematic of the CT between MoS_2 and WS_2 monolayers. (B) Energy-resolved transient absorption spectra of a MoS_2/WS_2 heterostructure and pure MoS_2 monolayer, excited by an optical pulse near the lower-energy MoS_2 A exciton energy. (C) Schematic of the CT between MoS_2 and $MoSe_2$ monolayers under 395 nm excitation. Blue and purple dots are differential reflection signals from 1L-MoS_2 and $MoS_2/MoSe_2$ heterostructure, respectively. (D) Coherent CT in $MoS_2/WS_2/MoSe_2$ trilayer heterostructure. (E) Twist angle dependence of the CT time and recombination lifetime. (A,B) Reproduced with permission from Reference 23. Copyright 2014, Nature Publishing group. (C) Reproduced with permission from Reference 38. Copyright 2014, American Chemical Society. (D) Reproduced with permission from Reference 39. Copyright 2017, American Chemical Society. (E) Reproduced with permission from Reference 40. Copyright 2017, American Chemical Society

authors only pumped the small bandgap MoS_2 and observed a photo-bleach signal of the large bandgap WS_2 that appears almost at the same time with the pump beam, corresponding to the ultrafast hole transfer process (an upper limit of 50 fs, Figure 3A,B).[23] It suggests that the CT happens in a much shorter time scale than the intralayer exciton lifetime (~few to tens of picoseconds).[41,42] Following the initial research study, several research groups made an effort to understand the mechanism further.[38,39,43] The study from Ceballos et al. identified electron (hole) transfer from $MoSe_2$ to MoS_2 (from MoS_2 to $MoSe_2$) at different exciting energies (Figure 3C).[38] The same group reported picosecond electron transfer in a trilayer heterostructure of $MoSe_2/WS_2/MoS_2$, indicating the coherent nature of the rapid CT processes (Figure 3D).[39] Moreover, a few more groups examined the rise and decay time of the transient transmission signal depending on the angle alignment between the two stacking crystal lattices.[40,44,45] From their observations based on heterostructures formed by either mechanically exfoliated or CVD synthesized monolayers, the ultrafast CT rate characterized by the rise time shows robustness against interlayer stacking configurations and thus momentum mismatch.[40,44] In contrast, the electron–hole recombination processes show a pronounced difference at various twist angles, as featured by different signal decay times (Figure 3E).[40] Surprisingly, the electron–hole recombination lifetime varies by almost three orders of magnitude from sample to sample (Figure 3E), but without a clear correlation with their twist angles. The charge recombination kinetics are independent of the excitation density or charge density, indicating defect-assisted electron–hole recombination as the dominant mechanism. From these experimental results, despite the significant interlayer momentum mismatch and the weak interlayer coupling, the CT at the 2D interface is ultrafast and happens at a time scale of 100 fs. In addition, minimizing the trap densities at the TMDC heterojunctions is also crucial to probe the intrinsic physics of momentum conservation in radiative interlayer exciton emission, which remains challenging for the community.

Photo-excited electron–hole pairs must dissociate into free carriers before efficient CT at vdWs interfaces. However, suppose one only considers the band edge offsets between CBM or VBM. In that case, the CT driving force is usually insufficient to overcome the exciton binding energies (~300 meV).[21,23,46,47] Although the CT directions are well-expected according to the band alignment predictions, the ultrafast dynamics is not easily understood

using traditional noncoherent CT picture.[48,49] In the perspective of Zhu and coauthors,[50] the difference between the molecular donor/acceptor interface and TMDC heterostructure interface is emphasized, that is, the delocalization in real space can dictate the charge separation at the molecular interfaces, but it may play the opposite role at 2D semiconductor heterostructures. In the following part, we briefly summarize some of the theoretical understanding of the mechanisms.

Several researchers have performed numerical calculations using time-dependent density-functional theory (TD-DFT) and proposed a coherent CT mechanism.[51–54] Wang et al. revealed an enhanced coupling between initial and final hole states in MoS_2 and WS_2 layer and concluded that the charged dipole layer is responsible for the unexpected rapid transfer of holes.[51] Long et al. proposed a slightly different picture, where the delocalization of the photo-excited states between the donor and acceptor materials assists in overcoming the electron–hole pair attraction and leads to efficient charge separation.[52] Besides, Li et al. compared the electron and hole transfer and electron–hole recombination across a MoS_2/WS_2 heterostructure and concluded that a longer quantum coherence favored faster CT, while the electron–hole recombination is much slower due to the strongly localized initial and final states within different layers.[53] Moreover, in the report from Wang et al., the coupling strengths for $\pm\mathbf{K}$, Γ_v, and Q_c valleys have been carefully compared, suggesting the strong layer mixing of Γ_v and Q_c valleys can mediate the twist angle-insensitive ultrafast interlayer CT.[54]

2.2 | The rising of interlayer excitons

Interlayer excitons, that is, bound electron–hole pair located separately in the adjacent materials, have been first pursued in GaAs coupled quantum wells[55] and widely studied for exciton Bose–Einstein condensation phenomena.[56] In type-II TMDC heterostructures, the ultrafast CT and the poorly screened Coulomb interaction give rise to interlayer excitons. Moreover, suitable bandgaps and extraordinary high binding energy for excitons in TMDC monolayers enable direct optical observations of the interlayer excitons at elevated temperatures, which initiates enormous research activities on this specific topic. In this part, we summarize contemporary research progresses of the interlayer excitons.

The interlayer excitons in semiconducting heterostructures with type-II band alignment were predicted as a direct resultant from interlayer CT.[57] Fang et al. have demonstrated a strong interlayer coupling between 2D interfaces, causing a spatially direct absorption but indirect emission, suggesting the formation of interlayer excitons.[58] Dr. Rivera and coauthors first reported the direct observation through PL and PL excitation (PLE) spectroscopies, featured as a reduced energy peak distinct from constituent monolayers in the PL spectrum associated with a much longer lifetime ~1.8 ns (Figure 4A).[27] Due to its out-of-plane dipole orientation, the vertical electric field is able to control the exciton properties, such as emission energy, luminescence intensity, diffusion length, and lifetime.[27,60–62] Although the CT process seems independent of the lattice orientation between constituent monolayers as aforementioned, the PL intensity of interlayer excitons displays a strong dependence on the twist angle, with the PL intensity reaching a maximum near 0° (60°) and gradually vanishing between 10° and 50°. This observation suggests that the formation of bright interlayer excitons requires finite interlayer hopping and kinetic energy, as expected by a theoretical simulation.[63] Then, a few following research works reported detailed temporal, excitation, and temperature dependence of the emission properties and analyzed the fine structure of the interlayer excitons to resolve momentum direct and indirect species.[64,65]

Another important feature making interlayer excitons more exciting is that they inherit the valley-contrasting property from monolayers (Figure 4B,C). Polarization-dependent PL measurements confirmed the presence of valley-polarized interlayer excitons, that is, ~30% valley-polarized interlayer exciton emission with circularly polarized excitation (Figure 4D). More importantly, the valley polarization lifetime can prolong by several orders of magnitudes under an external electric field (up to microsecond, Figure 4E).[59,66] Such a long lifetime allows for the visualization of a long lateral drift and diffusion carrying the valley polarization information over several micrometers.[59] Such generation and transport of valley-polarized excitons in heterojunctions stimulate further control and manipulation. For example, Unuchek et al. reported that the diffusion of valley-polarized excitons could be controlled and switched by an external electric field.[60,67] Ciarrocchi et al. have resolved two separate narrow interlayer transitions with opposite helicities, thus realizing a polarization switching device through electrical control.[68] These results make solid cases for their promising applications in next-generation photonic and valleytronic devices.

A twist and/or a difference in lattice constant between two stacking layers can give rise to a Moiré pattern with a superlattice potential.[69] This approach was applied to achieve unconventional superconducting in bilayer graphene[70,71] and led to the direct observation of Moiré excitons in WSe_2/WS_2,[72] $MoSe_2/WSe_2$,[73,74] and MoS_2/WS_2[75] heterojunctions with small twist angles, as

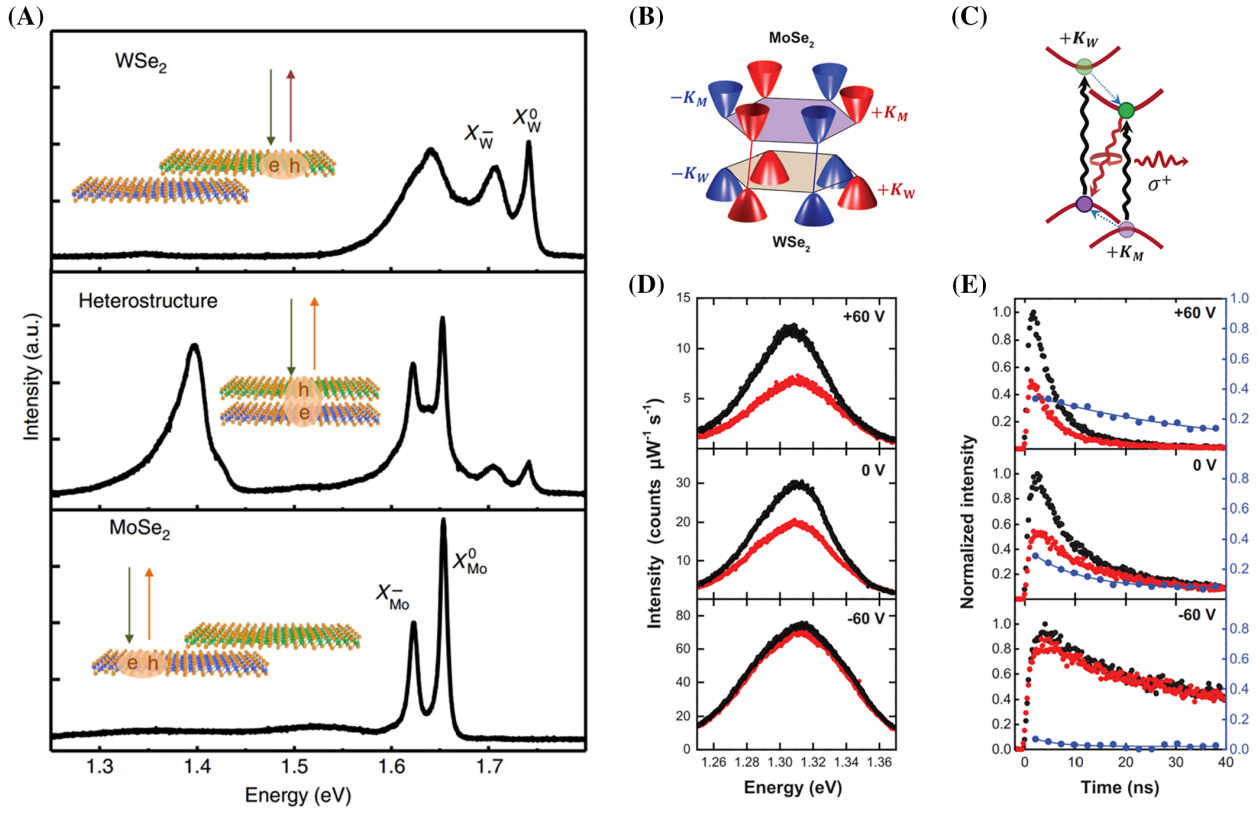

FIGURE 4 Interlayer exciton properties. (A) Observation of the interlayer exciton in $WSe_2/MoSe_2$ heterostructure. (B,C) Schematic of the valley polarization of the interlayer excitons. (D,E) Gate tuning of the valley polarization and lifetimes for the interlayer excitons. Black and red dots correspond to the same and opposite circular polarization between excitation and collection directions. Blue dots represent the degree of circular polarization. (A) Reproduced with permission from Reference 27. Copyright 2015, Nature Publishing group. (B–E) Reproduced with permission from Reference 59. Copyright 2016, American Association for the Advancement of Science

evidenced by the multiple emergent peaks either in the absorption or emission spectra. Besides, the Moiré-trapped interlayer excitons inherit the same valley-contrasting physics but with linewidths over 100 times narrower.[72] The technical details of these studies indicate that the twist angle and the stacking configuration are the key parameters. Weston et al. used atomic-resolution transmission electron microscopy to reveal the lattice reconstruction in heterojunction under different twist angles, reflecting the strikingly different structures in morphology and electronic properties.[76,77] The twist angles and the presence of Moiré potentials also show substantial modifications to the dynamics and diffusion of the interlayer excitons. It is worth noting that the impact of such Moiré potentials on both intralayer and interlayer excitons was suppressed at higher exciton density due to the shallow depth of the potential in the 2D landscape. However, this feature may benefit the successful engineering of the Moiré superlattices, which may open up a new area for exploring the novel quantum phenomenon. For example, Tang et al. tuned the Moiré excitons by a vertical electric field with the exciton energy-level anticrossing and oscillator strength redistribution, indicating the realization of a strong coupling regime.[78] Bai et al. reported the transfer of Moiré potentials from quantum-dot-like zero-dimensional traps into parallel stripes like 1D quantum wires by external strain, resulting in linearly polarized excitons in the 1D Moiré potentials.[79] So far, the study of Moiré physics under extreme conditions such as high magnetic field and high pressure is still lacking. Such experiments could provide useful information about the spin-valley dynamics in this new platform, which requires further exploration.

2.3 | CT in TMDC/graphene heterostructure

Ultrafast CT can also happen at the interface between the TMDC monolayer and the graphene, which typically occurs on the timescale of ~1 ps and motivates the applications in ultrafast photodetectors and all-optical modulators.[80–83] The preferred CT direction, from TMDC to graphene or vice versa, depends on the pumping

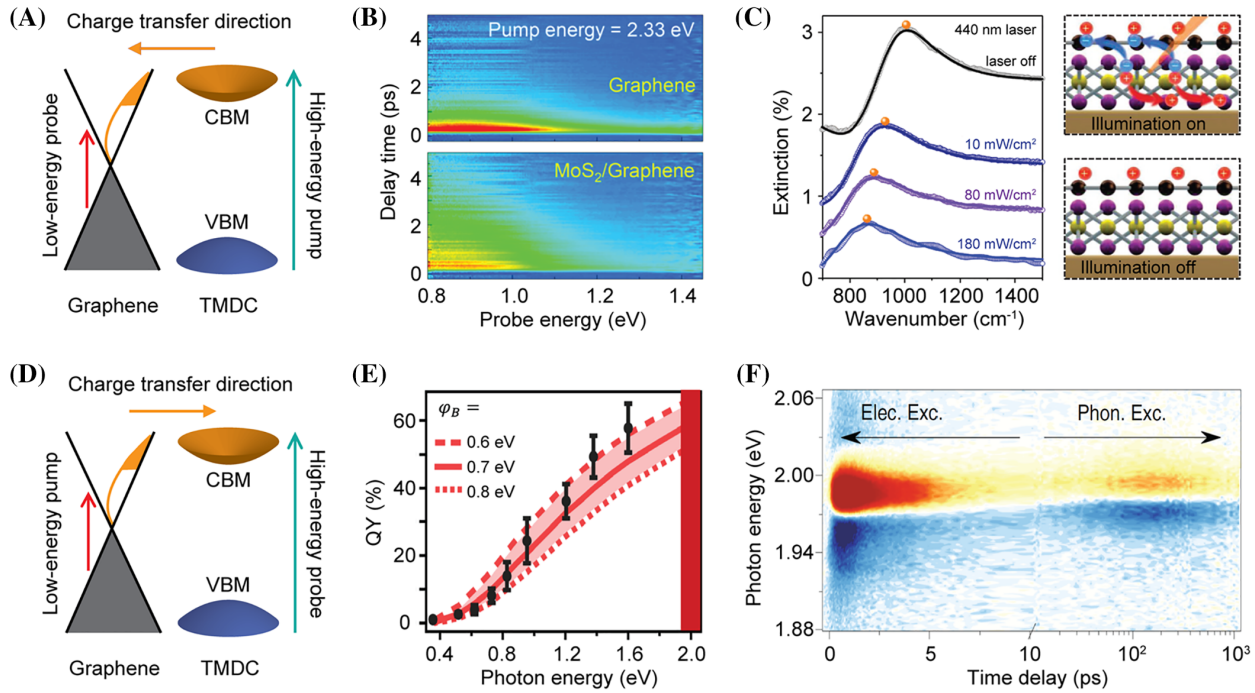

FIGURE 5 Ultrafast charge transfer (CT) at the transition metal dichalcogenide (TMDC)/graphene interface. (A) Schematic of the CT from the TMDC monolayer to graphene using the high-energy pump and low-energy probe. (B) Transient absorption spectra measured from bare graphene and MoS_2/graphene heterostructure with pump energy of 2.33 eV and probe energy of 0.8–1.4 eV. Compared to bare graphene, the heterostructure shows decelerated graphene hot carrier cooling dynamics due to the CT from MoS_2 to graphene. (C) Modulation of graphene plasmon via ultrafast CT from MoS_2 to graphene. (D) Schematic of the CT from graphene to TMDC via hot carrier injection using the low-energy pump and high-energy probe. (E) Quantum yield (QY) of hot electron injection in WS_2/graphene heterostructure measured as a function of the pump energy. (F) Photocarrier generation in WS_2/graphene heterostructure in the longer timescale (>100 ps) via acoustic phonon recycling. (B) Reproduced with permission from Reference 84. Copyright 2020, American Chemical Society. (C) Reproduced with permission from Reference 83. Copyright 2020, John Wiley and Sons. (E) Reproduced with permission from Reference 85. Copyright 2019, American Association for the Advancement of Science. (F) Reproduced with permission from Reference 86. Copyright 2020, Nature Publishing group

energy. As shown in Figure 5A, when the excitation energy is higher than the optical bandgap of the TMDC monolayer, the electrons in the TMDC monolayer can be efficiently pumped from the ground state to the excited state. Simultaneously, photoexcited carriers can also be generated in graphene but with limited carrier density due to its relatively low absorption. By integrating a MoS_2 monolayer with graphene to form the heterostructure, and monitoring the carrier relaxation in graphene using a low-energy probe, Lee et al. reported the deceleration of hot carrier cooling (by four times) in graphene induced by the nondissipative excited-state CT from the MoS_2 monolayer to the neighboring graphene (Figure 5B).[84] Such a CT direction leads to an increased photoexcited carrier population in graphene, slowing down the carrier cooling due to the enhanced hot optical phonon bottleneck effect. The slowed hot carrier cooling strategy has been widely adopted for boosting the maximum power conversion efficiency of photodetectors and solar cells. Dai et al. have recently demonstrated an efficient all-optical plasmonic modulator based on the same heterostructure and CT direction.[83] Graphene plasmons is excited with an infrared beam, while another visible light tune graphene plasmon in situ based on the ultrafast interfacial charge injection from photoexcited monolayer MoS_2, which efficiently modifies the doping level of graphene. Figure 5C clearly shows the modulation of graphene plasmon amplitude and frequency by changing the visible laser power. Benefitting from the ultrahigh photosensitivity of TMDC monolayer, the heterostructure modulator features low energy consumption. Plasmonic modulation of 44 cm^{-1} was achieved with a visible light illumination intensity of only 0.15 mW cm^{-2}.

On the other hand, when the excitation energy is not high enough to pump the TMDC directly (Figure 5D), the initial main excited state population will be hot carriers in graphene, which can quickly transfer to the TMDC side. The CT efficiency and dynamics can be conveniently probed in the high-energy range by monitoring the ground state bleaching signal at the TMDC exciton

resonance frequency. Hot carrier injection has been well investigated in metallic plasmonic-TMDC heterostructures.[87,88] For example, Wen et al. reported plasmonic hot carrier injection from gold nanorod into a WSe_2 bilayer. The injected hot carriers break the bilayer WSe_2's inversion symmetry and induce the second harmonic generation.[87,89–91] Compared to a noble-metal-based plasmonic system where the hot carrier excitation is efficient only around the plasmon resonance frequency, hot carriers in graphene can be excited efficiently with a wide range of pump energies due to its broad absorption range. The quantum yield (QY) of hot carrier injection from graphene into TMDC depends on the pump energy. For example, in the WS_2/graphene heterostructure, experimentally extracted QY increases from 0% to 60% when the pump energy increases from 0.4 to 1.6 eV, as shown in Figure 5E.[85] This QY enhancement stems from the thermalized hot carrier distribution, which depends on the pump energy and has a long tail toward higher energy due to electron–electron scattering. The hot carrier injection to the monolayer WS_2 is only allowed when the hot carrier energy overcomes the injection barrier determined by the energy alignment between graphene and the monolayer WS_2. In addition to the directly transferred graphene hot carrier, which gives rise to the bleaching signal at the A exciton resonance of the monolayer WS_2 in the timescale of shorter than 5 ps, Jiang et al. further observed a delayed bleaching signal in the timescale of longer than 100 ps (Figure 5F).[86] They attributed the delayed bleaching to the acoustic phonon recycling effect, which converts the photogenerated heat in graphene back into the carrier distribution in the monolayer WS_2 and enhances the overall photocarrier generation efficiency.

3 | ET IN 2D MATERIAL HETEROJUNCTIONS

ET is a physical process where the donor's excited state ETs to the acceptor's ground state. It is a nonradiative interaction that avoids the photon emission and reabsorption processes, thus maintaining high-energy conversion efficiency. According to the different interaction mechanisms, the ET processes can be divided into Förster and Dexter types, where the former relies on dipole–dipole coupling and interacts in a relatively long distance (<10 nm); and the latter establishes on charge exchange interaction and only works in the atomic proximity (≤1 nm). In this part, we review the state-of-art understanding of these two mechanisms at the 2D semiconductor heterojunctions.

3.1 | Förster-resonance ET

FRET, a process of transferring the excitons from an excited donor to an unexcited acceptor by nonradiative dipole–dipole interactions, is the underlying mechanism of numerous applications, including color tuning, biosensing, light-harvesting, and light generation. The FRET rate strongly depends on (1) the center-to-center separation between the donor and acceptor pair and (2) the Förster radius. Efficient FRET is limited typically to a length scale of approximate 10 nm due to the strong distance dependence of the process. This strong distance dependency can be modified by changing the acceptor geometry, for example, from a quantum dot (QD) ($k_{\mathrm{FRET}} \propto d^{-6}$) to a quantum well ($k_{\mathrm{FRET}} \propto d^{-4}$) (see Table 1).[92] It is worth mentioning that the FRET rate depends on the geometry and dimensionality of the acceptor and the effective dielectric constant of the donor (Table 2).[92] In the following, we briefly review the basics of FRET theory and focus on the 2D confinement case.

The FRET mechanism is illustrated by the band/energy level diagrams in Figure 6 schematically. This model only considers single donor-acceptor pair with a ground state $|0\rangle$ and an excited state $|\mathrm{exc}\rangle$. FRET requires the donor in the excited state. For example, absorbing a photon in the donor excites the electron into the higher excited states. Then, the hot electron relaxes into the lowest excited state by phonon scattering and bonds with the hole to form an exciton (typically in ps or sub-ps

TABLE 1 Generic distance dependence of the FRET rate given the acceptor's geometry (Adapted with permission from Reference 92, American Chemical Society)

Acceptor/Donor	Quantum dot (QD, 0D confinement)	Nanowire (NW,1D confinement)	Quantum well (QW, 2D confinement)
QD	QD → QD	QD → NW	QD → QW
NW	NW → QD	NW → NW	NW → QW
QW	QW → QD	QW → NW	QW → QW
Acceptor distance dependence	$k_{\mathrm{FRET,QD}} \propto \frac{1}{d^6}$	$k_{\mathrm{FRET,NW}} \propto \frac{1}{d^5}$	$k_{\mathrm{FRET,QW}} \propto \frac{1}{d^4}$

TABLE 2 Effective dielectrics summary

α-direction	Spherical (e.g., QD)	Cylindrical (e.g., NW)	Rectangular (e.g., QW)
X	$\varepsilon_{\mathrm{eff}_D}=\frac{\varepsilon_{\mathrm{QD}}+2\varepsilon_{\mathrm{M}}}{3}$	$\varepsilon_{\mathrm{eff}_D}=\frac{\varepsilon_{\mathrm{NW}}+\varepsilon_{\mathrm{M}}}{2}$	$\varepsilon_{\mathrm{eff}}=\varepsilon_{\mathrm{M}}$
Y	$\varepsilon_{\mathrm{eff}_D}=\frac{\varepsilon_{\mathrm{QD}}+2\varepsilon_{\mathrm{M}}}{3}$	$\varepsilon_{\mathrm{eff}}=\varepsilon_{\mathrm{M}}$	$\varepsilon_{\mathrm{eff}}=\varepsilon_{\mathrm{M}}$
Z	$\varepsilon_{\mathrm{eff}_D}=\frac{\varepsilon_{\mathrm{QD}}+2\varepsilon_{\mathrm{M}}}{3}$	$\varepsilon_{\mathrm{eff}_D}=\frac{\varepsilon_{\mathrm{NW}}+\varepsilon_{\mathrm{M}}}{2}$	$\varepsilon_{\mathrm{eff}}=\varepsilon_{\mathrm{M}}$

Note: The effective dielectric constants for QD, NW, and QW are expressed in the long-distance approximation. In this table, the main axis of the cylinder is considered to be along the *y*-direction. Adapted with permission from Reference 92, American Chemical Society.

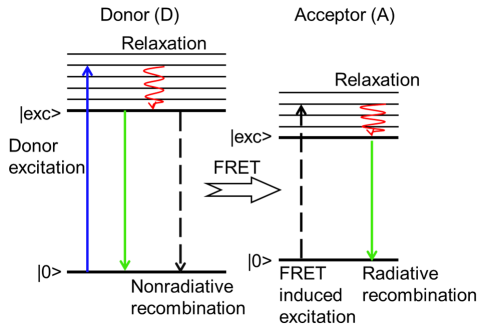

FIGURE 6 Schematic diagram of Förster resonance energy transfer (FRET). An electron is excited to a higher state (blue line) and relaxes to its lower excited state (red line). Green lines represent radiative recombination. Black dashed lines represent the nonradiative deexcitation (at the donor) and excitation (at the acceptor) via FRET

timescale). The formed exciton could transfer into the nearby acceptor nonradiatively via dipole–dipole coupling. The ET ratio is determined by the relative rate between the FRET and recombination.

The FRET rate can be calculated using Fermi's Golden Rule, which gives the probability of an exciton to be transferred from a donor to an acceptor, as expressed by

$$k_{\mathrm{FRET}}=\frac{2}{\hbar}\left\{\sum_f\left|\left\langle f_{\mathrm{exc}};0_{\mathrm{exc}}\middle|\widehat{V}_{\mathrm{int}}\middle|i_{\mathrm{exc}};0_{\mathrm{exc}}\right\rangle\right|^2\delta\left(\hbar\omega_{\mathrm{exc}}-\hbar\omega_f\right)\right\} \tag{1}$$

where $|i_{\mathrm{exc}};0_{\mathrm{exc}}\rangle$ is the initial state with an exciton in the donor and zero excitons in the acceptor; $|f_{\mathrm{exc}};0_{\mathrm{exc}}\rangle$ is the final state with an exciton in the acceptor and zero excitons in the donor; $\widehat{V}_{\mathrm{int}}$ is the exciton Coulomb interaction operator; $\hbar\omega_{\mathrm{exc}}$ and $\hbar\omega_f$ is the exciton's photon energy of the donor and acceptor, respectively. In a simplified model, the initial and final states can be written as $|i_{\mathrm{exc}};0_{\mathrm{exc}}\rangle=|i_{\mathrm{exc}}\rangle|0_{\mathrm{exc}}\rangle$ and $|f_{\mathrm{exc}};0_{\mathrm{exc}}\rangle=|f_{\mathrm{exc}}\rangle|0_{\mathrm{exc}}\rangle$, respectively, and Fermi's Golden Rule can be approximated by

$$k_{\mathrm{FRET}}\approx\frac{2}{\hbar}\left\{\sum_f\left|\left\langle f_{\mathrm{exc}}\middle|\widehat{U}_{\mathrm{int}}\middle|0_{\mathrm{exc}}\right\rangle\right|^2\delta\left(\hbar\omega_{\mathrm{exc}}-\hbar\omega_f\right)\right\} \tag{2}$$

where $\widehat{U}_{\mathrm{int}}=\langle 0_{\mathrm{exc}}|\widehat{V}_{\mathrm{int}}|i_{\mathrm{exc}}\rangle$ is the potential energy created by the exciton. With this approximation, Fermi's Golden Rule can be simplified using the fluctuation-dissipation theorem (FDT)[93,94]

$$k_{\mathrm{FRET}}=-\frac{2}{\hbar}\mathrm{Im}[dV\rho(\mathbf{r})\Phi_{\mathrm{int}}(\mathbf{r})] \tag{3}$$

Using the QD formalism developed in References 95 and 96, the final expression for the transfer rate is given by

$$k_{\mathrm{FRET}}=\frac{2}{\hbar}\mathrm{Im}\left[dV\left(\frac{\varepsilon_A(\omega)}{4\pi}\right)\mathbf{E}_{\mathrm{in}}(\mathbf{r})\cdot\mathbf{E}_{\mathrm{in}}^{*}(\mathbf{r})\right] \tag{4}$$

where the integration is taken over the acceptor volume, $\varepsilon_A(\omega)$ is the dielectric function of the acceptor, and $\mathbf{E}_{\mathrm{in}}(\mathbf{r})$ includes the effective electric field created by an exciton at the donor site. The electric field is calculated with $\mathbf{E}(\mathbf{r})=-\nabla\Phi(\mathbf{r})$ and the electric potential $\Phi(\mathbf{r})$, in CGS units, can be obtained by[97]

$$\Phi_\alpha(\mathbf{r})=\left(\frac{ed_{\mathrm{exc}}}{\varepsilon_{\mathrm{eff}_D}}\right)\frac{(\mathbf{r}-\mathbf{r}_0)\cdot\widehat{\boldsymbol{\alpha}}}{|\mathbf{r}-\mathbf{r}_0|^3} \tag{5}$$

where ed_{exc} is the dipole moment of the exciton and $\varepsilon_{\mathrm{eff}_D}$ is the effective dielectric constant of the donor, which depends on the geometry and the exciton dipole orientation, $\alpha=x,y,z$ (Table 2). The overall FRET rate is calculated as

$$k_{\mathrm{FRET}}=\frac{k_{x,\mathrm{FRET}}+k_{y,\mathrm{FRET}}+k_{z,\mathrm{FRET}}}{3} \tag{6}$$

where $k_{\alpha,FRET}$ is the FRET transfer rate for the α-exciton ($\alpha=x,y,z$).

For a 2D acceptor (QWs and 2D semiconductors) with thickness L_w embedded between two barriers with dielectric constant ε_{2D}. Two barriers have finite thickness L_l and semi-infinite thickness, respectively. Under the $L_w<<L_l$ limit, the electric potential can be written as[92,98]

$$\Phi_{2D}(\mathbf{r}) = \left(\frac{2\varepsilon_M}{\varepsilon_{2D}+\varepsilon_M}\right)\Phi_\alpha(\mathbf{r}) \quad (7)$$

Combining Equations (7) and (4), the FRET rate reduces to[92]

$$k_{\alpha,\mathrm{FRET}} = \frac{2}{\hbar}\left|\frac{2\varepsilon_M}{\varepsilon_{2D}+\varepsilon_M}\right|^2 \mathrm{Im}\left[{}_{2D}dS\left(\frac{\varepsilon_{2D}(\omega)}{4\pi}\right)\mathbf{E}_\alpha(\mathbf{r})\cdot\mathbf{E}^*_\alpha(\mathbf{r})\right] \quad (8)$$

Here the integration is over the surface of the 2D acceptor. Assuming that the 2D acceptor thickness is much smaller than the separation distance (d) between them, the FRET rate can be further simplified as[92,98]

$$k_{\alpha,\mathrm{FRET}} = \frac{2}{\hbar}b_\alpha\left(\frac{ed_{\mathrm{exc}}}{\varepsilon_{\mathrm{eff}_D}}\right)^2\frac{1}{d^4}\left|\frac{2\varepsilon_M}{\varepsilon_{QW}+\varepsilon_M}\right|^2 \mathrm{Im}[\varepsilon_{QW}(\omega_{\mathrm{exc}})] \quad (9)$$

where $b_\alpha = \frac{3}{16}, \frac{3}{16}, \frac{3}{8}$ for $\alpha = x,y,z$, respectively; and ε_M is the medium dielectric constant. It is worth noting that the scaling factor is proportional to $k_{\mathrm{FRET}} \propto 1/d^4$ in the 2D limit rather than $k_{\mathrm{FRET}} \propto 1/d^6$ in 3D confinement (see Table 1), thus theoretically enabling a stronger interaction and more pronounced long-range characteristics.

The FRET process in two donor-acceptor material systems, that is, 0D/2D material and 2D/2D material, have been widely studied. In most of the 0D/2D heterojunctions, 0D QDs, also known as nanocrystals, act as the donor due to their high optical absorption and QY, while 2D material is typically the acceptor.[99–103] In a pioneering work, Chen et al. studied the interaction between CdSe/ZnS QD and graphene.[104] The PL intensity of QD strongly quenches on graphene compared to quartz substrate (Figure 7A). Due to the screening effect of the insulating ligand shell, photoinduced CT is relatively slow and has a negligible effect.[105] However, the QD blinking effect resulting from the electron trapping between nanocrystal and substrate vanishes on graphene, suggesting that the quenching rate is significantly faster than the charge trapping rate. Thereby, the QD quenching is attributed to FRET, as further confirmed by the graphene

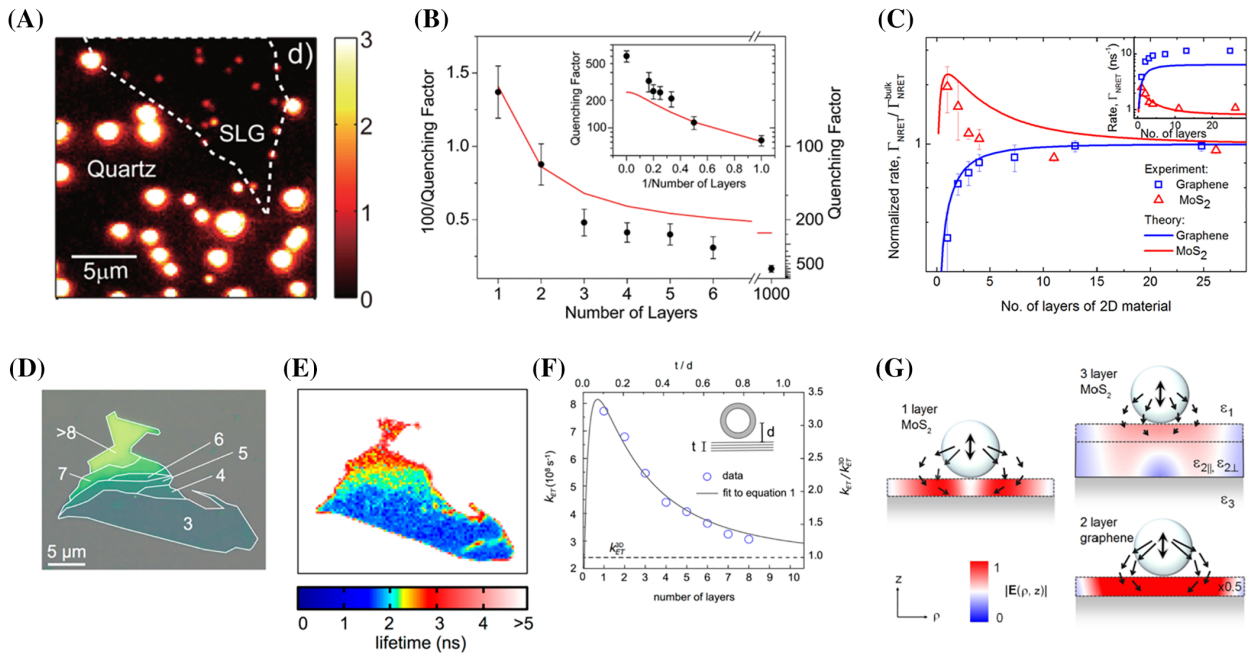

FIGURE 7 Energy transfer between quantum dot (QD) and 2D material. (A) PL image of individual CdSe/ZnS nanocrystals on 1L-graphene (SLG) and quartz. (B) Evolution of the PL quenching factor with the number of graphene layers. The black dots and red curve are experimentally obtained and theoretically calculated data, respectively. (C) Optical image of a mechanically exfoliated MoS_2 flake with indicated layer numbers. (D) QD PL lifetime mapping of the flakes shown in (C). (E) k_{FRET} as a function of the number of MoS_2 layers. The dashed line represents the ET rate to bulk-like MoS_2. Blue circles and solid curves are experimentally obtained and theoretically calculated data, respectively. (F) Normalized k_{FRET} from QDs to graphene and MoS_2 as a function of the layer thickness. The k_{FRET} on the respective bulk crystals uses for the normalization. Inset: Absolute rates of PL decay. (G) Numerical simulations of the electric field of a QD dipole inside the acceptor layers. The electric field in graphene is reduced by a factor of 2 for better comparison with MoS_2. (A, B) Reproduced with permission from Reference 104. Copyright 2010, American Chemical Society. (C–E) Reproduced with permission from Reference 103. Copyright 2014, American Chemical Society. (F,G) Reproduced with permission from Reference 102. Copyright 2016, American Chemical Society

thickness-dependent experiments and theoretical simulations (Figure 7B). Similarly, Prins et al. studied the interaction between CdSe/CdZnS QD and MoS_2, as shown in Figure 7C,D.[103] The PL lifetime mapping shows that the QD lifetime is much shorter on thin MoS_2 than the substrate. According to the formula $\eta_{ET} = 1 - \tau_{DA}/\tau_D$, in which η_{ET} is the FRET efficiency, τ_D and τ_{DA} is the lifetime of the donor on the bare substrate and in the heterojunction, respectively, η_{ET} is ~80% on few-layer MoS_2 and enhances to 98% on a monolayer MoS_2 (Figure 7E). Such high FRET efficiency stems from the reduced dielectric screening effect at the monolayer limit, making QD a perfect light absorption layer for 2D semiconductors. It is worth noting that the FRET rate (k_{FRET}) monotonically increases with the increasing graphene thickness and decreases with the increasing MoS_2 thickness (Figure 7F). Raja et al. systematically investigated this counterintuitive phenomenon and attributed it to the competition between screening and absorption of the QD dipole's electric field inside the acceptor layer.[102] To be specific, monolayer MoS_2 and bilayer graphene share similar thickness and absorption (imaginary part of the dielectric function), but the screening effect (real part of the dielectric function) in MoS_2 is much higher than graphene, leading to a much faster k_{FRET} on graphene than MoS_2 (Figure 7G). When the thickness increases, the screening of the electric field in MoS_2 is so strong that it induces the net decrease of k_{FRET}, while the screening of the electric field is much weaker in graphene than its absorption that induces a net increase of k_{FRET}. Based on the theoretical calculations, the authors established a model that can predict the k_{FRET} evolution with the acceptor layer thickness according to the material's dielectric function.

Due to the reduced dimension and the strong confinement induced in-plane dipole orientation in 2D semiconductors, the 2D/2D material system possesses a high geometry factor κ, and the dipole–dipole coupling strength is proportional to $1/d^4$ rather than $1/d^6$ in the molecular system (Equation 7), enabling a pronounced long-distance interaction. Kozawa et al. demonstrated an efficient FRET in a tightly contacted $WS_2/MoSe_2$ heterojunction.[106] Despite the type-II band alignment induced ultrafast charge separation and PL quenching, PLE spectroscopy shows that the $MoSe_2$ (acceptor) A exciton emission is enhanced when pumping energy is in resonance with WS_2 (donor) A and B exciton states (Figure 8A). The estimated ET rate is ~1 ps at low temperature, one of the fastest ET rates among all the donor-acceptor material systems. In the following work, Xu et al. systematically studied the effect of h-BN thickness on the CT/ET dynamics in WS_2/h-BN/MoS_2 heterojunction and found that ~4 layers are the optimal h-BN thickness for blocking CT and maintaining a high-efficiency ET level simultaneously. Unlike the typical down-conversion, in which ETs from the large bandgap material to the small one, the B exciton in MoS_2 (quasiparticle gap ~2.2 eV) enables the ET into WS_2 (quasiparticle gap ~2.4 eV) A exciton.[110,111] This counterintuitive ET direction reveals the complicated ET dynamics in 2D/2D system due to the band splitting induced multiple exciton states. With the reduced Coulomb screening effect and high intrinsic doping, the practical circumstances become even more complicated due to the formation of trion, spin-forbidden dark exciton, indirect exciton, and biexciton, especially at low temperatures.[112]

We systematically investigated the ET dynamics in WS_2/h-BN/$MoSe_2$ heterojunction to address the above concern. ~6 layers h-BN (~3 nm) is chosen as the spacer to block the CT and maintain the ET simultaneously.[107] In 1L-WS_2/h-BN/1L-$MoSe_2$ heterojunction, the $MoSe_2$ exciton emission doubles, while WS_2 trion emission quenches, indicating the ET donor is the trion in WS_2 rather than the exciton (Figure 8B). The PL lifetime measurements verify that WS_2 exciton lifetime is too short (<14 ps) to induce ET (~38 ps); while its trion lifetime is much longer (~57 ps) due to the difficulty for the electron dissociated from the trion to find an empty state in the conduction band during recombination.[113] The trion-mediated three-step FRET process is schematically drawn in Figure 8E, with (I) the formation of trions in WS_2 within 2 ps after optical excitation[113]; (II) ~40% trions recombining radiatively in WS_2 in ~57 ps; and (III) the other ~60% electron–hole pairs from the dissociated trions transferring into $MoSe_2$ in ~38 ps. Meanwhile, the electrons dissociated from the trions accumulate at the WS_2/h-BN interface to induce the optical gating effect, leading to the p-doping of $MoSe_2$ and the quenching of the trions (Figure 8B–E).[107]

Not limited to 2D TMDC heterojunction, Zhang et al. explored the FRET dynamics in 2D perovskite/2D TMDC.[114] The enhancement factor (EF) is defined as $EF = I_{DA}/I_A$, where I_{DA} and I_A are the PL intensity of the acceptor in the heterojunction and on the bare substrate, respectively. In $(C_6H_5C_2H_4NH_3)_2PbI_4/WS_2$ heterojunction, the WS_2 EF reaches up to ~8, which results from a collective contribution from both the closely contacted interface and the long-distance bulk states. Interestingly, the defect states at the interface between WS_2 and organic moiety offer another low-energy state to accept the energy transferred from both the bulk state in the perovskite and WS_2.

3.2 | Dexter-type energy transfer

DET,[115] also known as electron exchange ET, is a process within which two adjacent molecules exchange their

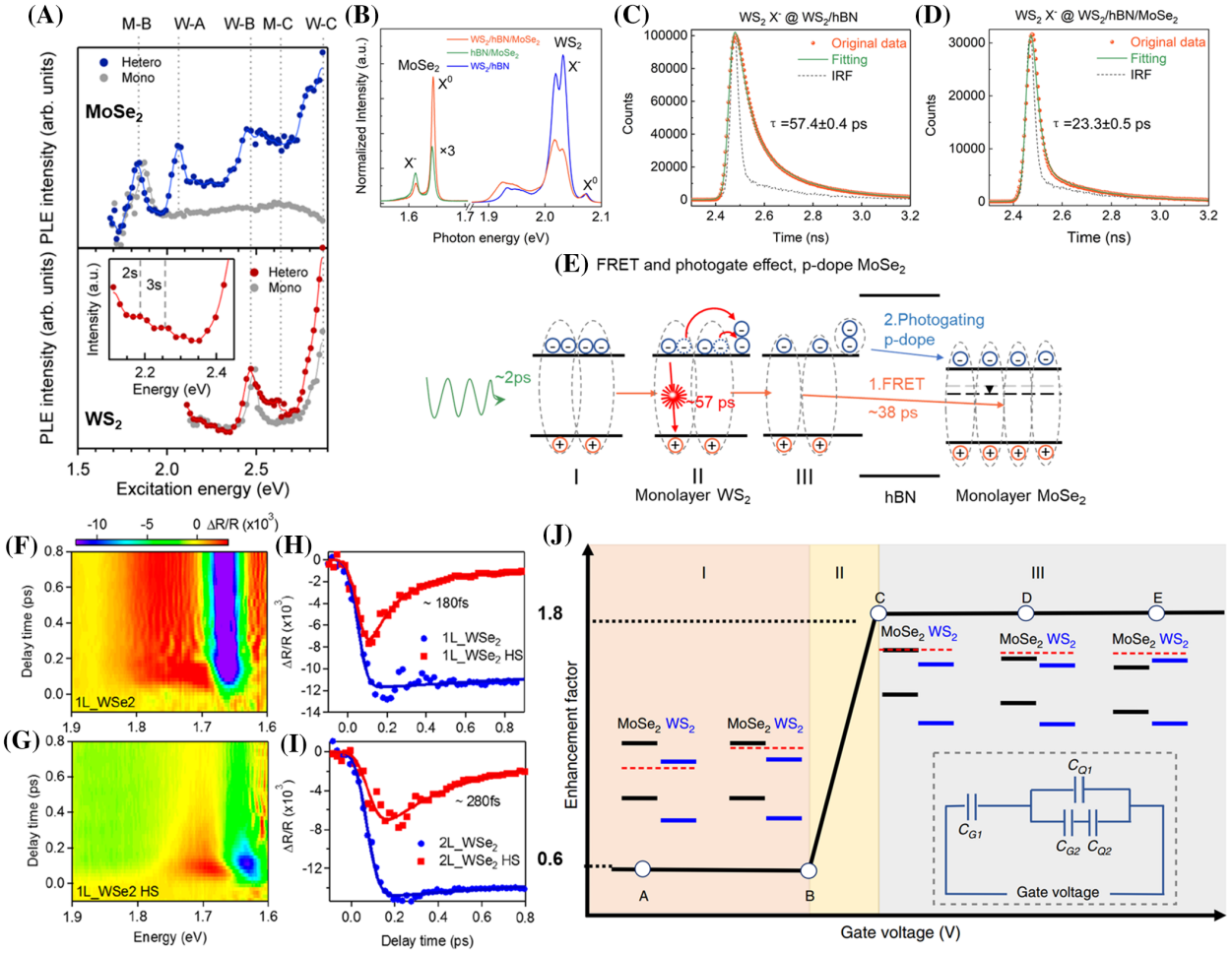

FIGURE 8 Energy transfer (ET) in 2D material heterojunctions. (A) PLE spectra for monolayer and heterojunction ($WS_2/MoSe_2$) at $MoSe_2$ A exciton (top panel) and WS_2 A exciton (bottom panel) emission energies at 1.61 and 1.98 eV, respectively. (B) PL spectra at WS_2/h-BN/$MoSe_2$, h-BN/$MoSe_2$, and WS_2/h-BN, respectively. (C,D) WS_2 trion lifetime at WS_2/h-BN and WS_2/h-BN/$MoSe_2$, respectively. (E) Schematic band diagrams and the dynamic processes in WS_2/h-BN/$MoSe_2$. The dashed line indicates the Fermi level. (F–I) Transient reflectance spectra of WSe_2-$MoTe_2$ heterostructures. Transient reflectance spectra for 1L-WSe_2 (F) and 1L-WSe_2/1L-$MoTe_2$ (G). (H,I) Comparison of A exciton bleach dynamics in 1L- (H) and 2L-WSe_2 (I) with their corresponding heterostructures. (J) The enhancement factor versus the gate voltage in the three different regions. Schematics of the heterojunction and the Fermi level are also shown. (A) Reproduced with permission from Reference 106. Copyright 2016, American Chemical Society. (B–E) Reproduced with permission from Reference 107. Copyright 2020, American Chemical Society. (F–I) Reproduced with from Reference 108. Copyright 2019, American Chemical Society. (J) Reproduced with permission from Reference 109. Copyright 2020, Nature Publishing Group

electrons based on the overlap of their wavefunctions (i.e., electron cloud), requiring the two emitters to be closely contacted (≤1 nm). In the vdWs heterojunction with type-I band alignment (Figure 1B), the electron and hole could transfer from the donor to the acceptor simultaneously after optical excitation and relaxation. DET can also occur between nonemissive electronic states of the materials, such as spin-forbidden triplet states. This exchange mechanism is based on the Wigner spin conservation rule, which includes: (1) singlet-singlet ET: $({}^1D* + {}^1A \xrightarrow{k_{DET}} {}^1D + {}^1A*)$; and (2) triplet-triplet ET: $({}^3D* + {}^1A \xrightarrow{k_{DET}} {}^1D + {}^3A*)$. The transfer rate of DET (k_{DET}) is given by $k_{DET} = KJ\exp\left(\frac{-2d}{L}\right)$,[116] where J is the normalized spectral overlap integral, K is an experimental constant, d is the distance between donor and acceptor, and L is the sum of vdWs radius of the donor and acceptor. Unlike the dipole–dipole coupling in FRET, which only allows the transfer of bright excitons, the mechanism of DET enables the transfer of both bright and dark excitons, thus offering a promising strategy to brighten the dark exciton in few-layer TMDCs toward high-efficiency ET. However, the DET results in TMDC heterojunctions have been rarely reported due to the difficulty to find a suitable type-I band alignment heterostructure. In a smartly designed $WSe_2/MoTe_2$ heterojunction with the type-I band alignment by Yamaoka

et al. and Wu et al., PLE spectra confirm that WSe_2 (donor) and $MoTe_2$ (acceptor) exciton emission intensities are quenched and enhanced with the above bandgap excitation in the heterojunction, supporting ET's existence.[108,117] In the transient reflectance spectra, the WSe_2 exciton bleaching signal in 1L-WSe_2 and 1L-WSe_2/1 L-$MoTe_2$ recovers at ~50 ps and ~180 fs, respectively, from which the calculated η_{ET} is ~99% (Figure 8F–H). 2L-WSe_2/1L-$MoTe_2$ exhibits similar transient reflectance results, as shown in Figure 8I. Since excitons in bilayer or thicker TMDCs are momentum-dark and forbid the FRET, the similar dynamic results between 1L- and 2L-WSe_2/$MoTe_2$ confirm the ET mechanism to be DET. WSe_2/black phosphorus (BP) heterojunction expands the DET dynamics into the mid-infrared regime (~450 meV). Notably, the BP PL in the heterojunction preserves the linear anisotropy due to the intrinsic anisotropic exciton emission.[118–120] A similar idea applies to organic semiconductor/TMDC heterojunction, in which pentacene (donor)/$MoSe_2$ (acceptor) heterojunction forms type-I band alignment. Zhang et al. demonstrated a ~86 times higher level of pump efficiency in the heterojunction than a single monolayer $MoSe_2$,[121] resulting from the high QY in pentacene and the ultrafast ET rate. Meanwhile, the pentacene's low dielectric constant reduces the screening effect in $MoSe_2$, thus increasing the trion binding energy from 23.4 (on SiO_2) to 28.3 meV.

Bellis et al. expanded the interfacial carrier dynamics from the vertically stacked to a laterally grown TMDC heterojunction composed of MoS_2 and $MoSe_2$ with a type-I band alignment.[122] By performing transient reflectance spectroscopy with both spatial and temporal resolution, the authors deduced the transfer velocity of both electrons and holes of ~10^4 m s^{-1}.[122] However, in the vertical heterojunction composed of the same materials, the same research group had reported ultrafast CT with the formation of indirect excitons.[38] The contradiction between the two cases may result from the different electronic band structures between the mechanically stacked and epitaxial grown heterostructure. To fully address the CT/ET dynamics in 2D heterostructures, advanced experimental techniques such as micro-angle-resolved photoemission spectroscopy that can resolve the interface band alignment are highly needed.

Since only a limited number of 2D heterojunction form type-I band alignment and exhibit efficient DET, many critical problems, for example, the transfer dynamics of spin-forbidden dark excitons and valley-polarized excitons, remain unexplored. Thereby, it is essential to engineer the band structure to enrich the donor-acceptor material components. The band structure of 2D materials can be tuned through either chemical or physical methods, as reported.[123–125] Meng et al. used a 3D ionic crystal LaF_3 as the substrate to impose a strong gating effect, thus shifting the Fermi level in WS_2/$MoSe_2$ heterojunction into WS_2's conduction band.[109] As a result, it blocks the electron transfer from $MoSe_2$ to WS_2 while preserves hole transfer from WS_2 to $MoSe_2$, leading to the sharp increase of EF from 0.6 to 1.8 (Figure 8J, point C). Furthermore, upon resonant excitation with WS_2 A exciton (~2 eV), the EF enhances to ~4 folds, revealing a highly efficient DET process (or the authors called exciton funneling effect in the original article).

4 | CT/ET IMPROVED PHOTODETECTOR

The integration of 2D materials into heterojunctions is not restricted by the lattice constant matching at the interface, thus enabling high degrees of device design and fabrication freedom. Since 2D materials belong to a specific type of "interface" materials, the optoelectronic performance of the heterojunctions is primarily determined by the carrier dynamics at the interface. This section uses the most widely studied device, that is, photodetector, to show the effect of interfacial CT/ET on the device performance optimization.[126–128]

The first strategy uses interfacial CT to tune the electrical and optical properties of the channel 2D semiconductor to improve the device performance. Lin et al. used Cs_2CO_3, a strong *n*-dopant, to functionalize the MoS_2 field-effect transistor (FET), leading to the enhanced electron concentration and mobility. Such anomalous enhancement in mobility is attributed to the screening of defect scattering centers by injecting electrons.[129–131] Meanwhile, the carrier lifetime is enhanced with the formation of trions, which induces a high optical gain, thus enhancing the photodetector responsivity by ~5 times. Similarly, the responsivity of Cs_2CO_3 decorated WSe_2 FET dramatically enhances by almost three orders of magnitudes.[132] Apart from the contributions mentioned above, the reduced effective Schottky barrier height between the metal contacts and WSe_2 also facilitates the effective collection of photogenerated electrons.

The second strategy to obtain a high-performance photodetector is to efficiently dissociate the photogenerated electron–hole pair using the built-in field at the junction. In a typical junction design, electrodes on different materials harvest the electrons and holes, respectively. In an upgraded photodetector configuration, Shin et al. designed a MoS_2/WSe_2 heterojunction, where electrodes both position on the MoS_2 channel layer that completely covers the underlying WSe_2 layer (Figure 9A).[133] As plotted in Figure 9B, the type-II band alignment leads to the accumulation of photogenerated electrons and holes in the MoS_2 and

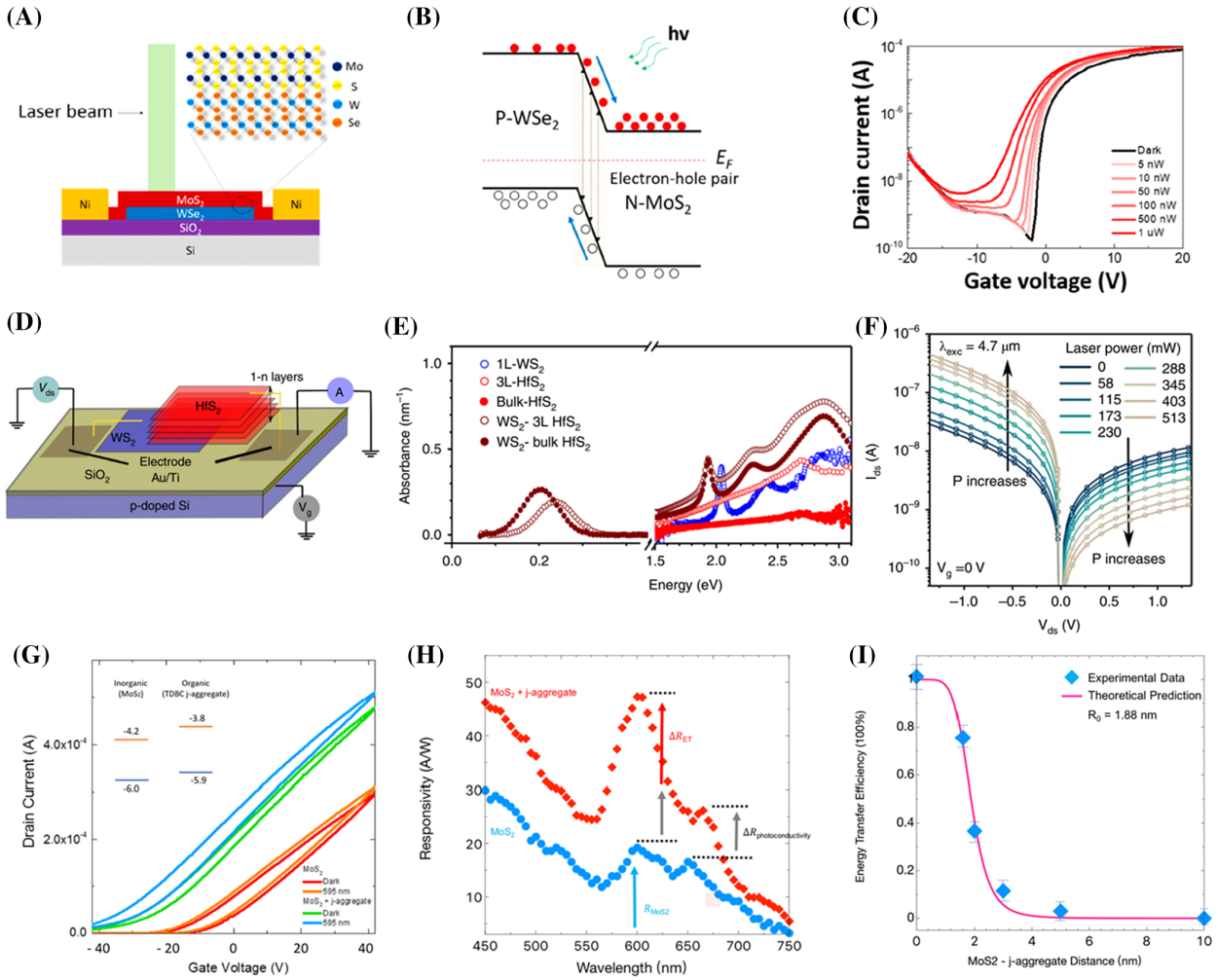

FIGURE 9 Charge/energy transfer improved photodetectors. (A–C) The schematic device structure (A), band alignment (B), and transfer characteristic (C) of the MoS_2/WSe_2 photodetector. (D–F) The schematic drawing (D), absorption spectrum (E), and *I–V* curve under 4.7 μm illumination (F) of the HfS_2/WS_2 interlayer exciton photodetector. (G–I) Transfer characteristic in the dark and under 595 nm illumination (G), Wavelength-dependent photoresponsivity (H), and the spacer thickness dependent ET efficiency (I) of the TDBC/MoS_2 device. (A–C) Reproduced with permission from Reference 133. Copyright 2020, American Chemical Society. (D–F) Reproduced with permission from Reference 134. Copyright 2020, Nature Publishing Group. (G–I) Reproduced with permission from Reference 135. Copyright 2018, American Chemical Society

WSe_2 layer, respectively. Thus, it only harvests the electrons in the MoS_2 channel layer. The accumulated holes in the WSe_2 layer induce the optical gating effect, which further enhances photogenerated electron concentration and lifetime, as evidenced by the successive negative shift of the transfer curve's threshold voltage with the increasing laser power (Figure 9C). Thus, the photodetector performance is vastly enhanced under illumination, achieving a high photoconductive gain of 10^6, a high photoresponsivity of 2700 $A\,W^{-1}$, a specific detectivity of 5×10^{11} Jones, and a moderate response time of 17 ms.[133] Not limited to higher device performance, CT has been utilized to expand the response wavelength in TMDC heterojunction using interlayer exciton as the absorber. Lukman et al. built a HfS_2/WS_2 heterojunction, which forms interlayer exciton with a large oscillation strength comparable to intralayer exciton.[134] Thus, the interlayer exciton state could directly absorb the photons with much smaller energy than the constituent semiconductors' bandgaps, expanding the operation wavelength to ~0.2 eV (mid-infrared) and could be further reduced to ~0.06 eV under gate voltage (Figure 9D,E). Besides, photogenerated electrons and holes accumulate rather than depleted at the interface, requiring external voltage to extract the free carriers. As shown in Figure 9F, under 4.7 μm illumination, a negative bias could increase the charge extraction with an enhanced photocurrent, while positive bias enhances the confinement of interlayer exciton and fewer extractable carriers. This prototype device shows superior

detectivity than other commercially available infrared photodetectors, especially at room or elevated temperatures.

ET could also improve photodetector performance. Cheng et al. fabricated a heterojunction composed of a j-aggregate thin film of organic dye (5,6-dichloro-2[3-[5,6-dichloro-1-ethyl-3-(3-sulfopropyl)-2(3H)-benzimidazolidene]-1-propenyl]-1-ethyl-3-(3-sulfopropyl) benzimidazolium hydroxide) (TDBC) and a 1L-MoS_2.[135] Both the dark and photo-conductivity improve with the deposition of j-aggregate, indicating efficient n-doping and ET (Figure 9G). The EF from ET is extracted from the wavelength-dependent photoresponsivity measurement, which has a maximum value of $93 \pm 5\%$ at 600 nm as a result of the near-perfect spectral overlap (Figure 9H). Furthermore, the experimentally deduced ET efficiency fits well with FRET theory by tuning the h-BN spacer thickness (Figure 9I), confirming that dipole–dipole coupling dominates the ET process. Since the ET timescale ranges from picoseconds to tens of picoseconds, it avoids any charge trapping processes at the interface, thus a promising strategy to achieve high responsivity and ultrafast response speed simultaneously (the highest reported response speed is 3 ps for MoS_2 photodetector[136]).

5 | CONCLUSIONS AND OUTLOOK

The recent progress on the understanding of charge and ET dynamics in vdWs heterojunction has been reviewed. The CT at vdWs heterojunctions is ultrafast due to the strong quantum coherence effect, showing great potential for ultrafast optical modulators. When two TMD layers are carefully aligned, the formed interlayer exciton with valley degree-of-freedom has innovated significant development in fundamental physics, including long-distance diffusion, Bose-Einstein condensates, and Moiré-excitons. However, most of the current works focus on the interlayer exciton between WS_2, MoS_2, $MoSe_2$, and WSe_2, forming between the K valleys in the Brillouin zone, thus strongly dependent on the stacking angle with weak oscillation strength. From a more practical point of view, interlayer exciton that forms at Γ point features high oscillation strength and is immune to the twist angle, thus expanding the optical absorption into the mid-infrared region.[134,137] The second part on ET has reviewed both the Förster and Dexter types. A comprehensive theoretical understanding of both mechanisms is given. One crucial parameter in the FRET dynamics is the dielectric function's real and imaginary parts, that is, screening and absorption of the electric field. Moreover, the quantum confinement effect and high intrinsic doping lead to various excitonic states with different lifetimes, which must be carefully treated in dealing with the dynamics. Recently, both weak and strong coupling regimes have been achieved between TMDC's exciton state and optical cavity mode.[138] Since the optical cavity mode can also manipulate FRET, it may achieve long-distance ET with ultra-high efficiency.[139] Various heterojunctions with type-I band alignment have been found to facilitate DET process. The ability to transfer and brighten the dark exciton makes it ideal for probing the dark states. However, current results are still limited to the momentum-dark excitons, whereas the spin-forbidden dark state remains unexplored. Finally, both CT and ET play important roles in optimizing the responsivity, speed, and operation wavelength of photodetectors.

In conclusion, the CT and ET in 2D material heterojunctions are determined by the band edge alignment and primarily affected by the band structure, relative dielectric function, stacking order, crystal orientation alignments, and the external electric/magnetic/optical/strain field. A clever design is critical to achieve the proposed functionality and study the underlying carrier dynamics. For example, inserting a thin insulating layer between two TMDC layers could block the CT, and keep the FRET almost intact. Interfacial CT and ET in vdWs heterojunctions set the foundation to explore the fundamental carrier dynamics and pave the way for practical device applications in ultrafast and high-performance optoelectronics.

ACKNOWLEDGMENTS

Qihua Xiong gratefully acknowledges strong support from the State Key Laboratory of Low-Dimensional Quantum Physics and start-up grant from Tsinghua University. Haiyun Liu gratefully acknowledges funding support from the National Natural Science Foundation of China (Grant No. 92056204). Hilmi Volkan Demir and Pedro Ludwig Hernández-Martínez gratefully acknowledge support from the National Research Foundation, Prime Minister's Office, Singapore under its Investigatorship Program (NRF-NRFI2016-08) and the Singapore Agency for Science, Technology and Research (A*STAR) SERC Pharos Program under Grant No. 152 73 00025. Hilmi Volkan Demir also acknowledges TUBA. Xue Liu acknowledges the financial support from the National Natural Science Foundation of China (12104006) and the start up fundations from Anhui University. Weigao Xu thanks the Fundamental Research Funds for the Central Universities in China (020514380231; 021014380177), the National Natural Science Foundation of China (21873048), the Natural Science Foundation of Jiangsu Province (BK20180319).

CONFLICT OF INTEREST

The authors declare no conflict of interest.

ORCID

Zehua Hu https://orcid.org/0000-0002-1185-2992
Haiyun Liu https://orcid.org/0000-0002-3584-4778

REFERENCES

1. Geim AK, Novoselov KS. The rise of graphene. *Nat Mater*. 2007;6(3):183-191.
2. Tan C, Cao X, Wu X-J, et al. Recent advances in ultrathin two-dimensional nanomaterials. *Chem Rev*. 2017;117(9):6225-6331.
3. Bellus MZ, Li M, Lane SD, et al. Type-I van der Waals heterostructure formed by MoS_2 and ReS_2 monolayers. *Nanoscale Horiz*. 2017;2(1):31-36.
4. Dean CR, Young AF, Meric I, et al. Boron nitride substrates for high-quality graphene electronics. *Nat Nanotechnol*. 2010;5(10):722-726.
5. Liu Y, Weiss NO, Duan X, et al. Van der Waals heterostructures and devices. *Nat Rev Mater*. 2016;1(9):1-17.
6. Geim AK, Grigorieva IV. Van der Waals heterostructures. *Nature*. 2013;499(7459):419-425.
7. Liu Y, Huang Y, Duan X, Der V. Waals integration before and beyond two-dimensional materials. *Nature*. 2019;567(7748):323-333.
8. Wang J, Han J, Chen X, Wang X. Design strategies for two-dimensional material photodetectors to enhance device performance. *InfoMat*. 2019;1(1):33-53.
9. Jin C, Ma EY, Karni O, Regan EC, Wang F, Heinz TF. Ultrafast dynamics in van der Waals heterostructures. *Nat Nanotechnol*. 2018;13(11):994-1003.
10. Zhang W, Wong PKJ, Zhu R, Wee ATS, Der V. Waals magnets: wonder building blocks for two-dimensional spintronics? *InfoMat*. 2019;1(4):479-495.
11. Liu S, Granados Del Aguila A, Liu X, et al. Room-temperature valley polarization in atomically thin semiconductors via chalcogenide alloying. *ACS Nano*. 2020;14(8):9873-9883.
12. Vandewal K, Albrecht S, Hoke ET, et al. Efficient charge generation by relaxed charge-transfer states at organic interfaces. *Nat Mater*. 2014;13(1):63-68.
13. Jortner J, Bixon M, Langenbacher T, Michel-Beyerle ME. Charge transfer and transport in DNA. *Proc Natl Acad Sci U S A*. 1998;95(22):12759-12765.
14. Schaibley JR, Yu H, Clark G, et al. Valleytronics in 2D materials. *Nat Rev Mater*. 2016;1(11):1-15.
15. Chhowalla M, Shin HS, Eda G, Li LJ, Loh KP, Zhang H. The chemistry of two-dimensional layered transition metal dichalcogenide nanosheets. *Nat Chem*. 2013;5(4):263-275.
16. Hu Z, Wu Z, Han C, He J, Ni Z, Chen W. Two-dimensional transition metal dichalcogenides: Interface and defect engineering. *Chem Soc Rev*. 2018;47(9):3100-3128.
17. Komsa H-P, Krasheninnikov AV. Electronic structures and optical properties of realistic transition metal dichalcogenide heterostructures from first principles. *Phys Rev B*. 2013;88(8):085318.
18. Terrones H, López-Urías F, Terrones M. Novel hetero-layered materials with tunable direct band gaps by sandwiching different metal disulfides and diselenides. *Sci Rep*. 2013;3(1):1-7.
19. Gong C, Zhang H, Wang W, Colombo L, Wallace RM, Cho K. Band alignment of two-dimensional transition metal dichalcogenides: application in tunnel field effect transistors. *Appl Phys Lett*. 2013;103(5):053513.
20. Fan Z, Wei-Bing Z, Bi-Yu T. Electronic structures and elastic properties of monolayer and bilayer transition metal dichalcogenides MX_2 (M=Mo, W; X=O, S, Se, Te): a comparative first-principles study. *Chin Phys B*. 2015;24(9):097103.
21. Chiu M-H, Zhang C, Shiu H-W, et al. Determination of band alignment in the single-layer MoS_2/WSe_2 heterojunction. *Nat Commun*. 2015;6(1):1-6.
22. Özcelik VO, Azadani JG, Yang C, Koester SJ, Low T. Band alignment of two-dimensional semiconductors for designing heterostructures with momentum space matching. *Phys Rev B*. 2016;94(3):035125.
23. Hong X, Kim J, Shi SF, et al. Ultrafast charge transfer in atomically thin MoS_2/WS_2 heterostructures. *Nat Nanotechnol*. 2014;9(9):682-686.
24. Froehlicher G, Lorchat E, Berciaud S. Charge versus energy transfer in atomically thin graphene-transition metal dichalcogenide van der Waals heterostructures. *Phys Rev X*. 2018;8(1):011007.
25. Ju L, Velasco J Jr, Huang E, et al. Photoinduced doping in heterostructures of graphene and boron nitride. *Nat Nanotechnol*. 2014;9(5):348-352.
26. Liu X, Pei J, Hu Z, et al. Manipulating charge and energy transfer between 2d atomic layers via heterostructure engineering. *Nano Lett*. 2020;20(7):5359-5366.
27. Rivera P, Schaibley JR, Jones AM, et al. Observation of long-lived interlayer excitons in monolayer $MoSe_2$-WSe_2 heterostructures. *Nat Commun*. 2015;6(1):6242.
28. Lazzeri M, Mauri F. Nonadiabatic Kohn anomaly in a doped graphene monolayer. *Phys Rev Lett*. 2006;97(26):266407.
29. Pisana S, Lazzeri M, Casiraghi C, et al. Breakdown of the adiabatic Born-Oppenheimer approximation in graphene. *Nat Mater*. 2007;6(3):198-201.
30. Zhao Y, Luo X, Li H, et al. Interlayer breathing and shear modes in few-trilayer MoS_2 and WSe_2. *Nano Lett*. 2013;13(3):1007-1015.
31. Chakraborty B, Bera A, Muthu DVS, Bhowmick S, Waghmare UV, Sood AK. Symmetry-dependent phonon renormalization in monolayer MoS_2 transistor. *Phys Rev B*. 2012;85(16):161403.
32. Miller B, Parzinger E, Vernickel A, Holleitner AW, Wurstbauer U. Photogating of mono-and few-layer MoS_2. *Appl Phys Lett*. 2015;106(12):122103.
33. Carrascoso F, Lin D-Y, Frisenda R, Castellanos-Gomez A. Biaxial strain tuning of interlayer excitons in bilayer MoS_2. *J Phys Mater*. 2019;3(1):015003.
34. Lu X, Luo X, Zhang J, Quek SY, Xiong Q. Lattice vibrations and Raman scattering in two-dimensional layered materials beyond graphene. *Nano Res*. 2016;9(12):3559-3597.
35. Tan Q-H, Sun Y-J, Liu X-L, et al. Observation of forbidden phonons, Fano resonance and dark excitons by resonance Raman scattering in few-layer WS_2. *2D Mater*. 2017;4(3):031007.

36. Fan S, Cao R, Wang L, et al. Quantum tunneling in two-dimensional van der Waals heterostructures and devices. *Sci China Mater*. 2021;64(10):1-29.
37. Xu W, Liu W, Schmidt JF, et al. Correlated fluorescence blinking in two-dimensional semiconductor heterostructures. *Nature*. 2017;541(7635):62-67.
38. Ceballos F, Bellus MZ, Chiu H-Y, Zhao H. Ultrafast charge separation and indirect exciton formation in a MoS_2-$MoSe_2$ van der Waals heterostructure. *ACS Nano*. 2014;8(12):12717-12724.
39. Ceballos F, Ju MG, Lane SD, Zeng XC, Zhao H. Highly efficient and anomalous charge transfer in van der Waals trilayer semiconductors. *Nano Lett*. 2017;17(3):1623-1628.
40. Zhu H, Wang J, Gong Z, Kim YD, Hone J, Zhu XY. Interfacial charge transfer circumventing momentum mismatch at two-dimensional van der Waals heterojunctions. *Nano Lett*. 2017;17(6):3591-3598.
41. Zhao J, Zhao W, Du W, Su R, Xiong Q. Dynamics of exciton energy renormalization in monolayer transition metal disulfides. *Nano Res*. 2020;13(5):1399-1405.
42. Palummo M, Bernardi M, Grossman JC. Exciton radiative lifetimes in two-dimensional transition metal dichalcogenides. *Nano Lett*. 2015;15(5):2794-2800.
43. Peng B, Yu G, Liu X, et al. Ultrafast charge transfer in MoS_2/WSe_2 P-N heterojunction. *2D Mater*. 2016;3(2):025020.
44. Ji Z, Hong H, Zhang J, et al. Robust stacking-independent ultrafast charge transfer in MoS_2/WS_2 bilayers. *ACS Nano*. 2017;11(12):12020-12026.
45. Wang K, Huang B, Tian M, et al. Interlayer coupling in twisted WSe_2/WS_2 bilayer heterostructures revealed by optical spectroscopy. *ACS Nano*. 2016;10(7):6612-6622.
46. Li Y, Cui Q, Ceballos F, Lane SD, Qi Z, Zhao H. Ultrafast interlayer electron transfer in incommensurate transition metal dichalcogenide homobilayers. *Nano Lett*. 2017;17(11):6661-6666.
47. Latini S, Winther KT, Olsen T, Thygesen KS. Interlayer excitons and band alignment in MoS_2/hBN/WSe_2 van der Waals heterostructures. *Nano Lett*. 2017;17(2):938-945.
48. Wasielewski MR. Photoinduced electron transfer in supramolecular systems for artificial photosynthesis. *Chem Rev*. 1992;92(3):435-461.
49. Marcus RA. Electron transfer reactions in chemistry. Theory and experiment. *Rev Mod Phys*. 1993;65(3):599-610.
50. Zhu X, Monahan NR, Gong Z, Zhu H, Williams KW, Nelson CA. Charge transfer excitons at van der Waals interfaces. *J Am Chem Soc*. 2015;137(26):8313-8320.
51. Wang H, Bang J, Sun Y, et al. The role of collective motion in the ultrafast charge transfer in van der Waals heterostructures. *Nat Commun*. 2016;7(1):1-9.
52. Long R, Prezhdo OV. Quantum coherence facilitates efficient charge separation at a MoS_2/$MoSe_2$ van der Waals junction. *Nano Lett*. 2016;16(3):1996-2003.
53. Li L, Long R, Prezhdo OV. Charge separation and recombination in two-dimensional MoS_2/WS_2: time-domain ab initio modeling. *Chem Mater*. 2017;29(6):2466-2473.
54. Wang Y, Wang Z, Yao W, Liu G-B, Yu H. Interlayer coupling in commensurate and incommensurate bilayer structures of transition-metal dichalcogenides. *Phys Rev B*. 2017;95(11):115429.
55. Islam MN, Hillman R, Miller DA, et al. Electroabsorption in GaAs/AlGaAs coupled quantum well waveguides. *Appl Phys Lett*. 1987;50(16):1098-1100.
56. Butov L, Lai C, Ivanov A, Gossard A, Chemla D. Towards Bose–Einstein condensation of excitons in potential traps. *Nature*. 2002;417(6884):47-52.
57. Fogler M, Butov L, Novoselov K. High-temperature superfluidity with indirect excitons in van der Waals heterostructures. *Nat Commun*. 2014;5(1):1-5.
58. Fang H, Battaglia C, Carraro C, et al. Strong interlayer coupling in van der Waals heterostructures built from single-layer chalcogenides. *Proc Natl Acad Sci U S A*. 2014;111(17):6198-6202.
59. Rivera P, Seyler KL, Yu H, et al. Valley-polarized exciton dynamics in a 2d semiconductor heterostructure. *Science*. 2016;351(6274):688-691.
60. Unuchek D, Ciarrocchi A, Avsar A, Watanabe K, Taniguchi T, Kis A. Room-temperature electrical control of exciton flux in a van der Waals heterostructure. *Nature*. 2018;560(7718):340-344.
61. Jauregui LA, Joe AY, Pistunova K, et al. Electrical control of interlayer exciton dynamics in atomically thin heterostructures. *Science*. 2019;366(6467):870-875.
62. Gao S, Yang L, Spataru CD. Interlayer coupling and gate-tunable excitons in transition metal dichalcogenide heterostructures. *Nano Lett*. 2017;17(12):7809-7813.
63. Yu H, Wang Y, Tong Q, Xu X, Yao W. Anomalous light cones and valley optical selection rules of interlayer excitons in twisted heterobilayers. *Phys Rev Lett*. 2015;115(18):187002.
64. Miller B, Steinhoff A, Pano B, et al. Long-lived direct and indirect interlayer excitons in van der Waals heterostructures. *Nano Lett*. 2017;17(9):5229-5237.
65. Baranowski M, Surrente A, Klopotowski L, et al. Probing the interlayer exciton physics in a MoS_2/$MoSe_2$/MoS_2 van der Waals heterostructure. *Nano Lett*. 2017;17(10):6360-6365.
66. Jiang C, Xu W, Rasmita A, et al. Microsecond dark-exciton valley polarization memory in two-dimensional heterostructures. *Nat Commun*. 2018;9(1):753.
67. Unuchek D, Ciarrocchi A, Avsar A, et al. Valley-polarized exciton currents in a van der Waals heterostructure. *Nat Nanotechnol*. 2019;14(12):1104-1109.
68. Ciarrocchi A, Unuchek D, Avsar A, et al. Polarization switching and electrical control of interlayer excitons in two-dimensional van der Waals heterostructures. *Nat Photon*. 2018;13(2):131-136.
69. Marcellina E, Liu X, Hu Z, et al. Evidence for Moiré trions in twisted $MoSe_2$ homobilayers. *Nano Lett*. 2021;21(10):4461-4468.
70. Cao Y, Fatemi V, Fang S, et al. Unconventional superconductivity in magic-angle graphene superlattices. *Nature*. 2018;556(7699):43-50.
71. Cao Y, Fatemi V, Demir A, et al. Correlated insulator behaviour at half-filling in magic-angle graphene superlattices. *Nature*. 2018;556(7699):80-84.
72. Jin C, Regan EC, Yan A, et al. Observation of Moiré excitons in WSe_2/WS_2 heterostructure superlattices. *Nature*. 2019;567(7746):76-80.
73. Tran K, Moody G, Wu F, et al. Evidence for Moiré excitons in van der Waals heterostructures. *Nature*. 2019;567(7746):71-75.

74. Seyler KL, Rivera P, Yu H, et al. Signatures of moire-trapped valley excitons in $MoSe_2/WSe_2$ heterobilayers. *Nature*. 2019; 567(7746):66-70.
75. Alexeev EM, Ruiz-Tijerina DA, Danovich M, et al. Resonantly hybridized excitons in Moiré superlattices in van der Waals heterostructures. *Nature*. 2019;567(7746):81-86.
76. Weston A, Zou Y, Enaldiev V, et al. Atomic reconstruction in twisted bilayers of transition metal dichalcogenides. *Nat Nanotechnol*. 2020;15(7):592-597.
77. Sung J, Zhou Y, Scuri G, et al. Broken mirror symmetry in excitonic response of reconstructed domains in twisted $MoSe_2/MoSe_2$ bilayers. *Nat Nanotechnol*. 2020;15(9):750-754.
78. Tang Y, Gu J, Liu S, et al. Tuning layer-hybridized Moiré excitons by the quantum-confined stark effect. *Nat Nanotechnol*. 2020;16(1):52-57.
79. Bai Y, Zhou L, Wang J, et al. Excitons in strain-induced one-dimensional Moire potentials at transition metal dichalcogenide heterojunctions. *Nat Mater*. 2020;19(10):1068-1073.
80. He J, Kumar N, Bellus MZ, et al. Electron transfer and coupling in graphene-tungsten disulfide van der Waals heterostructures. *Nat Commun*. 2014;5(1):5622.
81. Massicotte M, Schmidt P, Vialla F, et al. Picosecond photoresponse in van der Waals heterostructures. *Nat Nanotechnol*. 2016;11(1):42-46.
82. Yuan L, Chung T-F, Kuc A, et al. Photocarrier generation from interlayer charge-transfer transitions in WS_2-graphene heterostructures. *Sci Adv*. 2018;4(2):e1700324.
83. Guo X, Liu R, Hu D, et al. Efficient all-optical plasmonic modulators with atomically thin van der Waals heterostructures. *Adv Mater*. 2020;32(11):e1907105.
84. Tran MD, Lee SG, Jeon S, et al. Decelerated hot carrier cooling in graphene via nondissipative carrier injection from MoS_2. *ACS Nano*. 2020;14(10):13905-13912.
85. Chen Y, Li Y, Zhao Y, Zhou H, Zhu H. Highly efficient hot electron harvesting from graphene before electron-hole thermalization. *Sci Adv*. 2019;5(11):eaax9958.
86. Wei K, Sui Y, Xu Z, et al. Acoustic phonon recycling for photocarrier generation in graphene-WS_2 heterostructures. *Nat Commun*. 2020;11(1):3876.
87. Wen X, Xu W, Zhao W, Khurgin JB, Xiong Q. Plasmonic hot carriers-controlled second harmonic generation in WSe_2 bilayers. *Nano Lett*. 2018;18(3):1686-1692.
88. Dunklin JR, Rose AH, Zhang H, Miller EM, van de Lagemaat J. Plasmonic hot hole transfer in gold nanoparticle-decorated transition metal dichalcogenide nanosheets. *ACS Photonics*. 2019;7(1):197-202.
89. Wen X, Gong Z, Li D. Nonlinear optics of two-dimensional transition metal Dichalcogenides. *InfoMat*. 2019;1(3):317-337.
90. Du W, Zhao J, Zhao W, et al. Ultrafast modulation of exciton–plasmon coupling in a monolayer WS_2-Ag nanodisk hybrid system. *ACS Photonics*. 2019;6(11):2832-2840.
91. Yu H, Talukdar D, Xu W, Khurgin JB, Xiong Q. Charge-induced second-harmonic generation in bilayer WSe_2. *Nano Lett*. 2015;15(8):5653-5657.
92. Hernández-Martínez PL, Govorov AO, Demir HV. Generalized theory of forster-type nonradiative energy transfer in nanostructures with mixed dimensionality. *J Phys Chem C*. 2013;117(19):10203-10212.
93. Platzman PM, Wolff PA. *Waves and Interactions in Solid State Plasmas*. New York, NY: Academic Press; 1973.
94. Hua X, Gersten J, Nitzan A. Theory of energy transfer between molecules near solid state particles. *J Chem Phys*. 1985;83(7):3650-3659.
95. Govorov AO, Lee J, Kotov NA. Theory of plasmon-enhanced Förster energy transfer in optically excited semiconductor and metal nanoparticles. *Phys Rev B*. 2007; 76(12):125308.
96. Hernández-Martínez PL, Govorov AO. Exciton energy transfer between nanoparticles and nanowires. *Phys Rev B*. 2008; 78(3):035314.
97. Landau LD, Lifshitz EM. *Quantum Mechanics: Non-relativistic Theory*. Elsevier; 2013.
98. Hernández-Martínez PL, Govorov AO, Demir HV. Förster-type nonradiative energy transfer for assemblies of arrayed nanostructures: confinement dimension vs stacking dimension. *J Phys Chem C*. 2014;118(9):4951-4958.
99. Zang H, Routh PK, Huang Y, et al. Nonradiative energy transfer from individual Cdse/Zns quantum dots to single-layer and few-layer tin disulfide. *ACS Nano*. 2016;10(4):4790-4796.
100. Wang Z, Dong Z, Gu Y, et al. Giant photoluminescence enhancement in tungsten-diselenide–gold plasmonic hybrid structures. *Nat Commun*. 2016;7(1):1-8.
101. Sampat S, Guo T, Zhang K, et al. Exciton and trion energy transfer from giant semiconductor nanocrystals to MoS_2 monolayers. *ACS Photonics*. 2016;3(4):708-715.
102. Raja A, Montoya CA, Zultak J, et al. Energy transfer from quantum dots to graphene and MoS_2: the role of absorption and screening in two-dimensional materials. *Nano Lett*. 2016; 16(4):2328-2333.
103. Prins F, Goodman AJ, Tisdale WA. Reduced dielectric screening and enhanced energy transfer in single- and few-layer MoS_2. *Nano Lett*. 2014;14(11):6087-6091.
104. Chen ZYBS, Nuckolls C, Heinz TF, Brus LE. Energy transfer from individual semiconductor nanocrystals to graphene. *ACS Nano*. 2010;4(5):2964-2968.
105. Li S, Steigerwald ML, Brus LE. Surface states in the photoionization of high-quality CdSe core/shell nanocrystals. *ACS Nano*. 2009;3(5):1267-1273.
106. Kozawa D, Carvalho A, Verzhbitskiy I, et al. Evidence for fast interlayer energy transfer in $MoSe_2/WS_2$ heterostructures. *Nano Lett*. 2016;16(7):4087-4093.
107. Hu Z, Hernandez-Martinez PL, Liu X, et al. Trion-mediated forster resonance energy transfer and optical gating effect in WS_2/hBN/$MoSe_2$ heterojunction. *ACS Nano*. 2020;14(10): 13470-13477.
108. Wu L, Chen Y, Zhou H, Zhu H. Ultrafast energy transfer of both bright and dark excitons in 2D van der Waals heterostructures beyond dipolar coupling. *ACS Nano*. 2019;13(2): 2341-2348.
109. Meng Y, Wang T, Jin C, et al. Electrical switching between exciton dissociation to exciton funneling in $MoSe_2/WS_2$ heterostructure. *Nat Commun*. 2020;11(1):2640.
110. Hill HM, Rigosi AF, Rim KT, Flynn GW, Heinz TF. Band alignment in MoS_2/WS_2 transition metal dichalcogenide heterostructures probed by scanning tunneling microscopy and spectroscopy. *Nano Lett*. 2016;16(8):4831-4837.
111. Xu W, Kozawa D, Liu Y, et al. Determining the optimized interlayer separation distance in vertical stacked 2d WS_2:hBN: MoS_2 heterostructures for exciton energy transfer. *Small*. 2018;14(13):e1703727.

112. Bao D, del Águila AG, Do TTH, et al. Probing momentum-indirect excitons by near-resonance photoluminescence excitation spectroscopy in WS_2 monolayer. *2D Mater*. 2020;7(3):031002.
113. Singh A, Moody G, Tran K, et al. Trion formation dynamics in monolayer transition metal dichalcogenides. *Phys Rev B*. 2016;93(4):041401.
114. Zhang Q, Linardy E, Wang X, Eda G. Excitonic energy transfer in heterostructures of quasi-2D perovskite and monolayer WS_2. *ACS Nano*. 2020;14(9):11482-11489.
115. Dexter DL. A theory of sensitized luminescence in solids. *J Chem Phys*. 1953;21(5):836-850.
116. Valeur B. *Molecular Fluorescence: Principles and Applications*. Weinheim: Wiley-VCH; 2001.
117. Yamaoka T, Lim HE, Koirala S, et al. Efficient photocarrier transfer and effective photoluminescence enhancement in type I monolayer $MoTe_2/WSe_2$ heterostructure. *Adv Funct Mater*. 2018;28(35):1801021.
118. Zong X, Hu H, Ouyang G, et al. Black phosphorus-based van der Waals heterostructures for mid-infrared light-emission applications. *Light Sci Appl*. 2020;9(1):1-8.
119. Hu Z, Li Q, Lei B, et al. Water-catalyzed oxidation of few-layer black phosphorous in dark environment. *Angew Chem Int Ed*. 2017;56(31):9131-9135.
120. Hu Z, Li Q, Lei B, et al. Abnormal near-infrared absorption in 2D black phosphorus induced by Ag nanoclusters surface functionalization. *Adv Mater*. 2018;30(43):e1801931.
121. Zhang L, Sharma A, Zhu Y, et al. Efficient and layer-dependent exciton pumping across atomically thin organic-inorganic type-I heterostructures. *Adv Mater*. 2018;30(40):e1803986.
122. Bellus MZ, Mahjouri-Samani M, Lane SD, et al. Photocarrier transfer across monolayer MoS_2-$MoSe_2$ lateral heterojunctions. *ACS Nano*. 2018;12(7):7086-7092.
123. Han C, Hu Z, Gomes LC, et al. Surface functionalization of black phosphorus via potassium toward high-performance complementary devices. *Nano Lett*. 2017;17(7):4122-4129.
124. Wang Y, Xiao J, Zhu H, et al. Structural phase transition in monolayer $MoTe_2$ driven by electrostatic doping. *Nature*. 2017;550(7677):487-491.
125. Klein J, Wierzbowski J, Regler A, et al. Stark effect spectroscopy of mono- and few-layer MoS_2. *Nano Lett*. 2016;16(3):1554-1559.
126. Wang J, Hu W. Recent progress on integrating two-dimensional materials with ferroelectrics for memory devices and photodetectors. *Chin Phys B*. 2017;26(3):037106.
127. Bai G, Lyu Y, Wu Z, Xu S, Hao J. Lanthanide near-infrared emission and energy transfer in layered WS_2/MoS_2 heterostructure. *Sci China Mater*. 2019;63(4):575-581.
128. Wei X, Yan F-G, Shen C, Lv Q-S, Wang K-Y. Photodetectors based on junctions of two-dimensional transition metal dichalcogenides. *Chin Phys B*. 2017;26(3):038504.
129. Yang Q, Xue Y, Chen H, Dou X, Sun B. Photo-induced doping effect and dynamic process in monolayer $MoSe_2$. *J Semicond*. 2020;41(8):082004.
130. Lin JD, Han C, Wang F, et al. Electron-doping-enhanced trion formation in monolayer molybdenum disulfide functionalized with cesium carbonate. *ACS Nano*. 2014;8(5):5323-5329.
131. Wu Z, Luo Z, Shen Y, et al. Defects as a factor limiting carrier mobility in WSe_2: a spectroscopic investigation. *Nano Res*. 2016;9(12):3622-3631.
132. Lei B, Hu Z, Xiang D, et al. Significantly enhanced optoelectronic performance of tungsten diselenide phototransistor via surface functionalization. *Nano Res*. 2017;10(4):1282-1291.
133. Shin GH, Park C, Lee KJ, Jin HJ, Choi SY. Ultrasensitive phototransistor based on WSe_2-MoS_2 van der Waals heterojunction. *Nano Lett*. 2020;20(8):5741-5748.
134. Lukman S, Ding L, Xu L, et al. High oscillator strength interlayer excitons in two-dimensional heterostructures for mid-infrared photodetection. *Nat Nanotechnol*. 2020;15(8):675-682.
135. Cheng CH, Li Z, Hambarde A, Deotare PB. Efficient energy transfer across organic-2D inorganic heterointerfaces. *ACS Appl Mater Interfaces*. 2018;10(45):39336-39342.
136. Wang H, Zhang C, Chan W, Tiwari S, Rana F. Ultrafast response of monolayer molybdenum disulfide photodetectors. *Nat Commun*. 2015;6(1):1-6.
137. Ubrig N, Ponomarev E, Zultak J, et al. Design of van der Waals interfaces for broad-spectrum optoelectronics. *Nat Mater*. 2020;19(3):299-304.
138. Zhao J, Su R, Fieramosca A, et al. Ultralow threshold polariton condensate in a monolayer semiconductor microcavity at room temperature. *Nano Lett*. 2021;21(7):3331-3339.
139. Coles DM, Somaschi N, Michetti P, et al. Polariton-mediated energy transfer between organic dyes in a strongly coupled optical microcavity. *Nat Mater*. 2014;13(7):712-719.

AUTHOR BIOGRAPHIES

Zehua Hu received his Bachelor's degree in Physics from Nanjing University in 2014, and PhD degree in physics from the National University of Singapore in 2018. He is currently a research fellow in Nanyang Technological University. His research interests include optical spectroscopy and optoelectronics in low-dimensional semiconducting materials, especially the ultrafast carrier dynamics in the heterojunctions.

Xue Liu received his PhD in Physics from Tulane University in 2017. From 2017 to 2020, he worked as a postdoctoral research fellow at Nanyang Technological University, Singapore. He is currently a full professor in the Institutes of Physical Science and Information Technology at Anhui University. His research interests include electric and optoelectronic properties of low

dimensional materials and heterostructures, and their applications in next generation functional devices.

Qihua Xiong is a Professor of Physics at Tsinghua University, Fellow of American Physical Society and Optical Society of America. He received his PhD from Penn State University in 2006, and then conducted postdoctoral research at Harvard University. From 2009 to 2020, he worked at Nanyang Technological University. His group is specialized in optical spectroscopy investigations of light-matter interactions in low-dimensional quantum matter. He currently serves as Associate Editor for Nano Letters, Journal of Semiconductors and Chinese Physics B, and international advisory board or editorial board for many prestigious journals, such as ACS Photonics, Nano Research, Science China Materials, eSciences, and so on.

How to cite this article: Hu Z, Liu X, Hernández-Martínez PL, et al. Interfacial charge and energy transfer in van der Waals heterojunctions. *InfoMat*. 2022;4(3):e12290. doi:10.1002/inf2.12290